STUDY OF DUST PROPERTIES AROUND HELIX NEBULA(NGC–7293) USING IRIS, AKARI, WISE SURVEYS, AND 2-DUST MODEL

A Dissertation

Submitted to the Dean Office, Institute of Science & Technology Tribhuvan University, Kirtipur in the Partial Fulfillment for the Requirement of Master's Degree of Science in Physics

By

Raju Paudel

May 30, 2023

Recommendation

It is certified that Mr. Raju Paudel has carried out the dissertation work entitled **"STUDY OF DUST PROPERTIES AROUND HELIX NEBULA(NGC–7293) USING IRIS, AKARI, WISE SURVEYS, AND 2-DUST MODEL"** under our supervision. We recommend the dissertation in partial fulfillment of the requirement of a Master's Degree of Science in Physics at Tribhuvan University.

. . . . . .

(Supervisor)

Assoc. Prof. Dr. Ajay Kumar Jha

Tribhuvan University,

Kirtipur, Nepal

Date: . . . . . .

Acknowledgements

I would like to express my deep gratitude to the Institute of Science and Technology at Tribhuvan University for providing me with a valuable opportunity to conduct this research. I am immensely grateful to my supervisor, Assoc. Prof. Dr. Ajay Kumar Jha, and co-supervisors, Assoc. Prof. Dr. Ajay Mishra and Lecturer Devendra Raj Upadhyay, for their diligent guidance and encouragement in completing this work. I am also appreciative of the Department of Physics at Amrit Campus and the helpfulness and cooperation of the administrative and library staff.

I would like to acknowledge UGC for providing me with funds to conduct this research and the various software and websites that were instrumental in my research, including SkyView Virtual Observatory, SIMBAD, Gaia Archive, Python 3.7, Excel, and Aladin v10. Furthermore, I would like to thank my family and friends for their unwavering love and support throughout this endeavor. I am particularly grateful to my friend, Saroj Ray, for his constant support and invaluable assistance. Finally, I extend my heartfelt thanks to all those who assisted me directly or indirectly in the preparation of this dissertation.

Raju Paudel

EVALUATION

This is to certify that we have evaluated this dissertation work entitled **"STUDY OF DUST PROPERTIES AROUND HELIX NEBULA(NGC–7293) USING IRIS, AKARI, WISE SURVEYS, AND 2-DUST MODEL"**, submitted by Mr. Raju Paudel and in our opinion, it fulfills all the specified criteria, in the scope and quality, as the dissertation in the partial fulfillment for the requirement of Master's Degree of Science in Physics at Tribhuvan University.

Evaluation committee

Assoc. Prof. Dr. Ajay Kumar Jha
Supervisor
Central Department of Physics

Prof. Dr. Leela Pradhan Joshi
Head of Department of Physics
Amrit Campus

Asst. Prof. Pitamber Shrestha
M. Sc. Coordinator
Department of Physics,
Amrit Campus
Tribhuvan University

External Examiner

Internal Examiner

Date: . . . . . .

Abstract

The present study aims to investigate the properties of the dust around Helix Nebula (NGC 7293) using IRIS, AKARI, and WISE surveys and the 2-Dust model. Helix Nebula is one of the well-known planetary nebulae in our Milky Way Galaxy. The study objectives include examining the dust color temperature, dust mass distribution, distribution of flux, and Jean's criteria of the nebula, producing dust color temperature and dust mass maps of the field, and determining the mass loss rate, luminosity, inner shell radius, outer shell radius, and other dust properties of Helix Nebula using a density distribution function and comparing them to another model. The methodology employed includes using 2-Dust code, Aladin v10.0, and Python 3.7. The FITS image was taken from Sky View Virtual Observatory. The study findings indicate that the relative flux density is maximum around the central region and minimum around the outer region at F100 μm and F22 μm FITS images. The dust particle that emits a flux of 140 μm is minimum in the central region. The dust color temperature of Helix Nebula varies depending on the survey used, with an average dust color temperature of (28.930 ± 0.005) K for the IRIS survey, (24.440 ± 0.078) K for the AKARI survey, and (277.490 ± 0.001) K for the WISE survey. The study also found that the dust color temperature was higher in the WISE survey than in the IRIS and AKARI surveys, suggesting an inverse relationship between the dust color temperature and the wavelength. The dust mass value was found to be higher in the AKARI survey and lower in the WISE survey. The calculated dust mass of Helix nebula using IRIS, AKARI, and WISE survey was found to be 0.10 $M_\odot$, 0.56 $M_\odot$, and 0.034 $M_\odot$ respectively. The estimated dust mass in the circumstellar shell was 0.051 $M_\odot$ and the mass loss rate was found to be 1.04×10^{-5} $M_\odot$ yr^{-1} using the axisymmetric model. The study concludes that the results obtained from the 2- Dust code as well as the IRIS, AKARI, and WISE surveys provide a better understanding of the properties of dust around Helix Nebula.

Contents

Chapter 1

Introduction

1.1 Overview

Human beings are the advanced civilization of the universe at the present times. We are trying to find the other civilizations in the universe by using space science technology. Our origin and existence are mysterious, so we are searching for our origin and existence. Our origin and existence correlate to the origin of universe formation and evolution of galaxies, the interstellar medium (ISM), nebulae, and the solar system. Studying nebulae has become a very active field of astrophysical research as we now have a better understanding of how they are involved in the life cycle of stars. Nebulae are where stars and planets are born, so they play a crucial role in their evolution. Planetary nebulae, in particular, are the main contributors to the end of a star's life cycle. This research focuses on investigating the dust properties of the Helix Nebula (NGC 7293) using data from IRIS, AKARI, and WISE surveys, as well as the 2-Dust model of the nebula.

1.2 Interstellar Dust

Dust can be found in all astrophysical environments, from planetary shells and disks to spiral, elliptical, starburst, and active galaxies, as well as in pre-galactic objects such as QSO (Quasi-Stellar Objects) absorption lines and damped Lyα systems. Interstellar dust In HII regions, the dust temperature is usually around 70-100 K. With the development of infrared astronomy in the 1970s, it became possible to observe all of these sources of dust. Infrared radiation from the nuclei of normal and active galaxies is also predominantly

thermal radiation from dust, making thermal dust emission one of the most significant sources of infrared radiation in astronomy dramatically alters galaxies' spectral appearance and interpretation of their underlying physical properties as a result of its presence [1]. Before 1930, it was believed that space was completely transparent, and that light could travel infinitely without being absorbed or scattered. Trumpler's work challenged this assumption [2]. He looked at the dispersion of open clusters, which are groups of freshly created stars present in a huge molecular cloud, throughout his research. For a given wavelength (λ), the distance (r) magnitude (m the apparent and M the absolute) relationship is given by,

$$m_\lambda - M_\lambda = 5log\frac{r}{10pc} + A_\lambda \tag{1.1}$$

where $A_\lambda \geq 0$ denotes the radiation losses (extinction) caused by the intervening medium. Assume the medium's opacity is uniform throughout all distances and directions, and A_λ may be represented as,

$$A_\lambda = a_\lambda r \tag{1.2}$$

A constant known as a_λ was introduced in the work of Aller and Trumpler (1939) to describe the average extinction of light in the galactic plane, which they determined to be 0.79 mag/kpc in photographic magnitudes. The amount of extinction caused by interstellar dust particles is significant and depends on the direction of observation. The current average extinction value of 2 mag/kpc means that the extinction over a 5 kpc distance is 10 magnitudes. The dust particles that cause extinction have sizes comparable to the wavelength of light and efficiently scatter light. Gas can also cause extinction, but its efficiency per unit mass is much lower. Scattering by gas is negligible in interstellar space due to the low total amount of gas allowed by the Oort limit. Interstellar particles can cause extinction in two ways.

- During absorption, the energy of the light is absorbed by the dust particles and converted into heat. This heat is then emitted at infrared wavelengths that correspond to the temperature of the dust particles.
- Scattering causes a change in the direction of light propagation, which results in a decrease in intensity in the original direction of propagation.

In this study, we derive and examine an equation for interstellar extinction. We make the assumptions that the size of the particles, the index of refraction of the medium, and the number density of the particles are already determined. For the sake of simplicity, we also assume that all particles are spherical with the same radius (a) and the geometric cross-section of (πa^2). The actual extinction cross-section of the particles (C_{ext}) is given by the following expression:

$$C_{\text{ext}} = Q_{\text{ext}} \pi a^2 \tag{1.3}$$

The extinction efficiency factor is denoted by C_{ext}. Let's say we have a small block of space that has a length of dl and a cross-section of dA, perpendicular to the direction of light. We assume that the dust particles inside the block do not block each other. If the density of dust particles in the block is n, then the number of particles in the block is n dl dA. These particles will block a fraction of the area dA, which is known as the optical depth, denoted by $d\tau$ where,

$$d\tau = \frac{n dA dl C_{\text{ext}}}{dA} = n C_{\text{ext}} dl \tag{1.4}$$

As a result, the intensity within the length dl is modified by the following factor:

$$dI = -I d\tau \tag{1.5}$$

The quantity $d\tau$ can be referred to as optical depth. The overall optical depth from the star to Earth is determined by the integral of $d\tau$ over the entire path.

$$\tau(r) = \int_0^r d\tau = \int_0^r n C_{\text{ext}} dl = C_{\text{ext}} \bar{n} r \tag{1.6}$$

The symbol $\bar{n}$ represents the average density of particles along a specific path. The magnitude of extinction can be calculated using the following equation:

$$A = (2.5 log e)\tau \tag{1.7}$$

and hence

$$A(r) = (2.5 log e) C_{\text{ext}} \bar{n} r \tag{1.8}$$

It is possible to use this formula in reverse to determine the particle density, given that the other variables are known. The extinction efficiency factor Q_{ext} can be accurately calculated for spherical particles of a specific radius a and refractive index μ. However, in general, the exact calculation of Q_{ext} is complex and may require numerical methods.

$$Q_{\text{ext}} = Q_{\text{abs}} + Q_{\text{sca}} \tag{1.9}$$

The extinction efficiency factor, Q_{ext}, can be expressed as the sum of the absorption efficiency factor, Q_{abs}, and the scattering efficiency factor, Q_{sca}. If we introduce the following notation:

$$x = \frac{2\pi a}{\lambda} \tag{1.10}$$

Here, λ denotes the wavelength of the radiation. With this notation, the expression for Q_{ext} becomes:

$$Q_{\text{ext}} = Q_{\text{ext}}(x, \mu) \tag{1.11}$$

The exact expression for Q_{ext} is a series expansion in x, where the convergence of the series becomes slower for larger values of x. When x is much smaller than 1, the process is known as Rayleigh scattering, while for larger x, it is called Mie scattering. Figure 1.1 depicts the dependence of Q_{ext} on x for refractive indices of 1.5 and 1.33. For very large particles, where x is much larger than 1, Q_{ext} is equal to 2, which is twice the value that one would expect based solely on the geometry of the particle. This discrepancy arises due to the diffraction of light at the edges of the particle. In addition to extinction, interstellar dust can also cause other observable phenomena, such as the reddening of starlight. This phenomenon occurs because the amount of extinction increases for shorter wavelengths of light. As light travels through interstellar space, its extinction increases as the wavelength decreases from red to ultraviolet. This means that the light of distant stars appears redder than expected based on their spectral class, which is determined by the relative strengths of spectral lines not affected by extinction.

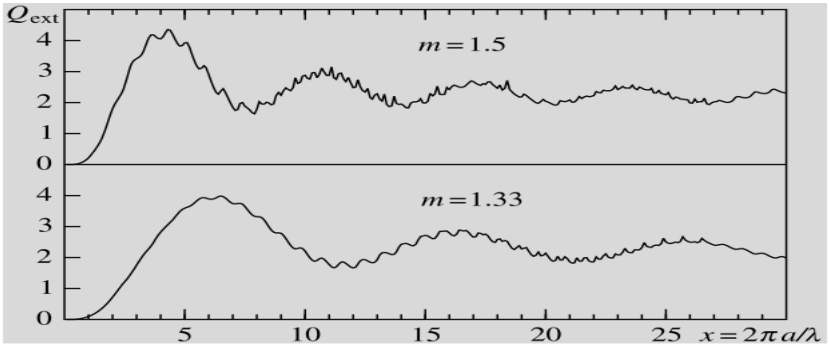

Figure 1.1: Mie scattering is the extinction efficiency factor for spherical particles with refractive indices of 1.5 and 1.33 (water's refractive index). The horizontal axis is proportional to particle size, as defined by x = 2πa/λ, where an is the particle radius and λ is the wavelength of the radiation [3].

Here, we will discuss the interstellar extinction curve. We can express Equation (1.1) for a star that is observed with two filters, having wavelengths λ_1 and λ_2 as follows [3]:

$$m_{\lambda 1} - M_{\lambda 2} = 5log\frac{r}{10pc} + A_{\lambda 1} \tag{1.12}$$

and

$$m_{\lambda 1} - M_{\lambda 2} = 5log\frac{r}{10pc} + A_{\lambda 2} \tag{1.13}$$

Subtracting equation (1.13) from (1.12) we get,

$$(m_{\lambda 1} - m_{\lambda 2} = (M_{\lambda 2} - M_{\lambda 2}) + (A_{\lambda 1} - A_{\lambda 2}) \tag{1.14}$$

If we consider the blue filter with $\lambda_1 = m_{\lambda_1}$ and visible filter with $\lambda_2 = m_{\lambda_2}$, then equation (1.14) becomes:

$$(B - V) = (M_B - M_V) + (A_B - A_V) \tag{1.15}$$

Here, (B - V) represented the color index. At the surface of the star, $A_B = A_V = 0$, above equation reduces to

$$(B - V)_0 = (M_B - M_v) \tag{1.16}$$

Using equation (1.16) in equation (1.15) We get,

$$(B - V) - (B - V)_0 = (A_B - A_V) \tag{1.17}$$

In equation (1.17), the left-hand side is represented by (E_{B-V}) called the color excess. Therefore,

$$E_{B-V} = A_B - A_V \tag{1.18}$$

Let's consider a third wavelength $\lambda_3 = \lambda$, then the wave equation can be used to calculate the color excess, which is given by:

$$E_{\lambda-V} = A_\lambda - A_V \tag{1.19}$$

Dividing equation (1.19) by (1.18)

$$\frac{E_{\lambda-V}}{E_{B-V}} = \frac{A_\lambda - A_V}{A_B - A_V} \tag{1.20}$$

$$\frac{E_{\lambda-V}}{E_{B-V}} = \frac{A_\lambda}{A_B - A_V} - R \tag{1.21}$$

Where,

$$R = \frac{A_v}{A_B - A_V} \tag{1.22}$$

Which is called the fiducial ratio.

The interstellar extinction curve is a plot between the normalized selective extinction or the normalized total absorption and the reciprocal of the wavelength. The normalized selective extinction is given by the ratio of the selective extinction to the total extinction, while the normalized total absorption is given by the ratio of the total absorption to the total extinction. Figure 1.2 displays a typical interstellar extinction curve for R = 3.1.

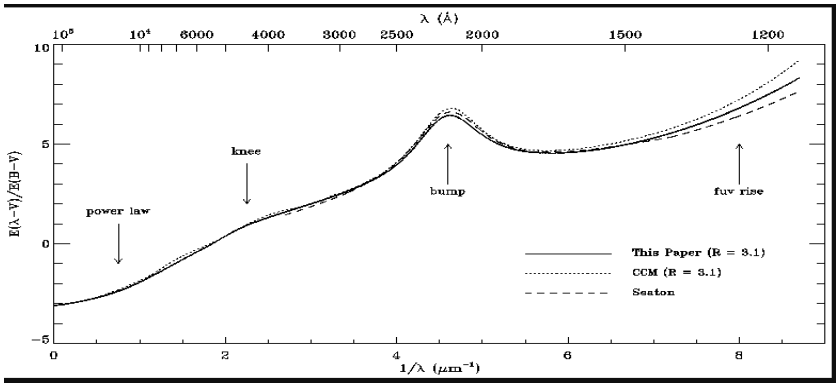

Figure 1.2: The interstellar extinction curve [4].

The extinction curve of interstellar dust shows a ”toe” region in the far infrared and a linear region up to the ”knee” in the near-infrared. The IRAS band covers the toe to the knee region, while the optical band covers the knee to the bump region, which follows a power law. The maximum extinction occurs at the bump region with a wavelength of 217 nm. Smaller dust particles produce higher extinction in the ultraviolet region. The interstellar extinction curve is uniform in all directions of the Milky Way. Microwaves, sub-mm, and radio waves are not affected by the presence of interstellar dust, and gamma rays cannot be absorbed or scattered by it. Thermal radiation emitted by interstellar dust accounts for the far and near-infrared radiation that we observe.

Cardelli and colleagues discovered that the dust particles in interstellar space range in size from 5 μm to 0.1 μm or even smaller. The smaller dust particles cause the maximum extinction in the ultraviolet region. Additionally, there are smaller dust particles present. The extinction pattern observed in interstellar space helps establish a connection between extinction in the ultraviolet, optical, and infrared regions [5]. Astrophysicists have determined that water ice, silicates, and potentially graphite are present in interstellar dust by examining the peaks of the extinction curve. The size of the dust grains can be inferred from their scattering properties, and they are typically smaller than one micrometer. The strongest scattering occurs from grains of approximately 0.3 μm, but smaller particles are also believed to exist. The dust grains form in the atmospheres of late spectral type stars such as K and M. Gas condenses into grains, similar to how water in the Earth's atmosphere forms snow and ice. Radiation pressure expels the grains into interstellar space. It is also possible for grains to be created during the formation of stars or directly from atoms and molecules present in interstellar clouds.

Apart from explaining interstellar extinction, there are several other reasons why dust is studied in astrophysics. Firstly, even though dust grains constitute only about 1% of the total mass of the interstellar medium, they are responsible for about 30% of the total luminosity of the galaxy in the form of thermal emission in the infrared. Secondly, dust grains serve as a surface on which molecules are formed, especially H_2, which is formed more efficiently on dust surfaces compared to gas-phase reactions. Thirdly, dust plays a vital role in the thermal balance of astrophysical processes such as star formation. Dust is involved in the formation and evolution of stars and planetary systems as stars are born within cocoons of dust and gas. The presence of dust may catalyze the gravitational collapse of

protostars, providing an efficient radiator of excess heat energy [6]. Protoplanetary discs have been observed around young stars due to the extinction and emission arising from the dust they contain.

Strong shock waves in the warm phases of the interstellar medium primarily destroy dust. This destruction is caused by sputtering, which is the removal of atoms from a solid surface due to the impact of high-energy particles, and vaporization caused by high-velocity collisions between grains. These processes return grain material to the gas phase. Additionally, shattering from collisions between grains significantly alters the size distribution of the remaining grains [7]. The interstellar grains not only scatter radiation but also absorb it, causing them to emit radiation at infrared wavelengths that correspond to their temperatures. The typical temperature of dust in interstellar space, including dark nebulae, is about 10–20 K, which corresponds to a wavelength range of 300–150 μm according to Wien's displacement law. However, if the dust is located near a hot star, its temperature may rise to 100–600 K and the maximum emission will shift to a shorter wavelength range of 30–5 μm [7]. In HII regions, the dust temperature is usually around 70-100 K. With the development of infrared astronomy in the 1970s, it became possible to observe all of these sources of dust. Infrared radiation from the nuclei of normal and active galaxies is also predominantly thermal radiation from dust, making thermal dust emission one of the most significant sources of infrared radiation in astronomy.

In this chapter, the basic theory of interstellar dust is discussed.

The second chapter describes the basic types of the nebula, details of the Helix Nebula, some parameters, and formulas required in this thesis, some surveys, objectives, and motivation.

Chapter three presents the data reduction and obtaining processes required to analyze the IR images and analyze tools.

Four chapters present the resulting data set and describe how it appears.

Finally, Chapter Five concludes this work and suggestions further work.

Chapter 2

Theory

2.1 Nebula

A nebula is a large, cloudy area in space primarily composed of hydrogen and helium gas, along with dust. These formations can occur when a dying star, such as a supernova, expels gas and dust, resulting in the formation of multiple nebulae. Nebulae are commonly found in interstellar or intergalactic space and some act as ”star nurseries” by facilitating the birth of new stars. Steven R. Coe classified nebulous or cloudy objects in the sky into five types, which are dark nebulae, emission nebulae, reflection nebulae, supernova remnants, and planetary nebulae [8].

- Reflection Nebulae are clusters of dusty clouds that reflect light from neighboring stars and often serve as the birthplace of new stars. They appear blue in color because blue light scatters more efficiently. Examples of reflection nebulae include ic-2631 and VdB1.

- Emission Nebulae are composed of high-temperature gas clouds that emit radiation when their atoms become excited by ultraviolet light from nearby stars. These nebulae often give birth to stars or contain actively forming ones, producing a range of colors depending on the atoms involved. Examples of emission nebulae include the Eagle Nebula and NGC 6726.

- Dark Nebulae are composed of dust clouds that obscure light from objects behind them. They are similar in composition to reflection nebulae but appear different due to the angles of the light source, cloud, and observer. Dark nebulae are often found

in conjunction with reflection and emission nebulae, spanning several hundred light-years in diameter. Examples of dark nebulae include NGC 2264 and the Horsehead Nebula.

- Supernova Remnants are formed when a massive star explodes at the end of its life, creating a brilliant light display. These remnants can power an entire galaxy for several days, and typical supernova remnants have a diameter of only a few light-years. Examples of such nebulae include the Crab Nebula, Puppis A, and others.

- Planetary Nebulae: Planetary Nebulae are shells of gas that are expelled by dying stars, representing the second-to-last stage of stellar evolution for stars that range in mass from one to eight solar masses. They have a lifespan of approximately 100,000 years and resemble planets in small telescopes, but are named as such only due to their appearance. The typical size of a planetary nebula is less than one light-year, and examples include M57 (the Ring Nebula), M27 (the Dumbbell Nebula), and the Helix Nebula (NGC 7293), which are discussed briefly in sections 2.2 and 2.3.

2.2 Stellar Evolution of Planetary Nebulae

”Planetary Nebula” is misleading because it does not actually involve a planet. The name was given by Sir William Herschel who observed that it appeared like a fuzzy greenish patch similar to outer planets through small telescopes. Planetary Nebulae are the final stage in the life cycle of intermediate-mass stars, which have a main sequence mass of 1 to 8 solar masses and follow similar evolutionary paths. These stars burn hydrogen to helium in their core for most of their lives until the core can no longer support hydrogen burning and moves into a shell around it. As the star moves away from the red giant branch of the H-R diagram, the mass of the helium core steadily increases until it ignites. The star then moves towards the horizontal branch until the helium burning is forced into a shell, and at this point, it moves up the asymptotic giant branch. The star at this stage is unstable to dynamic pulsations due to hydrogen and helium burning in shells around a core of carbon, nitrogen, and oxygen. The pulsations increase in amplitude until the material achieves escape velocity, and once the material starts to escape, the remaining atmosphere becomes less stable, and ejection continues until the hydrogen-rich zone is completely ejected [9]. Planetary nebulae are limited to a specific range of star masses. Only stars with a core mass

of around 0.6 solar masses undergo the necessary evolutionary process to form planetary nebulae. The white dwarf that remains after mass ejection becomes hot enough to ionize the surrounding material while it is still in close proximity to the star. Stars with larger masses evolve at a faster rate, resulting in a shorter visibility period as planetary nebulae. Conversely, smaller stars do not reach the required temperature before the surrounding material disperses too widely, preventing the formation of a planetary nebula [10]. The lifespan of a planetary nebula is estimated to be around 10,000 years, determined by analyzing its expansion velocities, surface brightness, and sizes. Theoretical models, such as the interacting wind model, have been proposed to explain the observations of planetary nebulae. This model suggests that the atmosphere of an extended red giant star is ejected, forming the nebula, and a fast wind generated by the remaining white dwarf collides with the nebular material, compressing it into a spherical shell. Multiple rings seen in some planetary nebulae may result from several episodes of slow massive winds followed by sweeping by fast winds. The diverse shapes of planetary nebulae can be explained by variations in the mass loss rate and velocity as functions of latitude on the central star [11]. As the central star progresses through its evolutionary stages and its temperature rises, the properties of the planetary nebula it creates may shift from being ionization bounded to density bounded. In a density-bounded nebula, all of the material is ionized, and photons with energies greater than the 13.6 electron volts required to ionize hydrogen can leave the nebula without being absorbed. Conversely, an ionization bounded nebula is surrounded by a neutral shell, and all of the ionizing photons are absorbed within the nebula. As it evolves, a planetary nebula may transition from being ionization bounded to density-bounded over time.

This research is about studying the dust and 2-Dust model of the Helix Nebula, a planetary nebula that is close to Earth and easy to observe. The Helix Nebula has a simple structure and low density, which makes it a good subject for learning how planetary nebulae form. Also, its central white dwarf star provides important information about how stars evolve. We will talk more about the Helix Nebula later in the text.

2.3 Helix Nebula (NGC–7293)

The planetary nebula (PN) phase is one of the last stages of development for intermediate-mass stars, with a mass range of 0.5 to 8 solar masses. Planetary nebulae form when a star evolves and leaves the main sequence, passes through the red giant and asymptotic giant branch (AGB) phases, and eventually becomes a white dwarf. The white dwarf emits intense UV radiation that heavily ionizes the area around it, producing atomic emissions. This area is surrounded by a mixture of neutral and ionized atomic and molecular gas, and dust that the star expelled during its AGB and proto-planetary nebula (PPN) phases [12]. The envelope is clumpy, with dense globules of gas and dust providing conditions that are suitable for molecular existence.

More than 1,800 planetary nebulae have been categorized in the Milky Way Galaxy, with Helix Nebula (NGC–7293) being one of the most extensively studied. Also known as Caldwell 63, it is located in the Aquarius constellation and is a brilliant planetary nebula that is one of the closest to Earth [13]. Its angular extent in the sky is massive at 1000", and the Gaia mission has calculated its distance to be 199.505 ±1.7394 pc. These features make it a highly desirable target for telescopes on the ground and in space across a wide range of wavelengths. The Helix has been studied using Hubble and Spitzer space telescopes in optical and infrared wavelengths, as well as the Infrared Space Observatory (ISO). Radio telescopes like the VLA, CSO, KP 12 m, and Sub-millimeter Telescope (SMT) have also observed the Helix at centimeter to sub-millimeter wavelengths [14].

The Helix Nebula is shaped like a flattened spheroid with a concentration of matter along the equatorial plane, tilted at an angle of about 21^o to 37^o from our viewpoint. The inner disk is 8×19 arcmin (0.52 pc) in size, the outer torus is 12×22 arcmin (0.77 pc), and the outermost ring is around 25 arcmin (1.76 pc) in diameter. The outermost ring appears flattened on one side due to its collision with the surrounding interstellar medium [15]. The entire planetary nebula structure is believed to have expanded in the previous 6,560 years, and the inner disk in the last 12,100 years. The outer ring expands at a pace of 40 km/s, whereas the inner disk expands at roughly 32 km/s [16].

The Helix Nebula was the first known planetary nebula with cometary knots. Its primary ring contains nebulosity knots, which have recently been discovered in several surrounding planetary nebulae, particularly those with a molecular envelope, such as the Ring and Dumbbell Nebulae [17]. The knots in the Helix Nebula are symmetric in a radial pattern

emanating from the central star (CS). They are called ”cometary” knots and each has a core of neutral molecular gas. They also have strong photoionization fronts or cusps toward the central star and tails extending away from it [18]. All of the tails radiate out from the Planetary Nebulae Nucleus (PNN). Each knot, excluding the tails, is roughly the size of the Solar System. The Helix Nebula contains over 40,000 cometary knots [19]. The knots are most likely caused by the Rayleigh-Taylor instability. The ionized inner nebula, which has a low density and a fast expansion velocity, is accelerating the denser, slower expanding, predominantly neutral material that was lost earlier when the star was on the Asymptotic Giant Branch [20]. The temperature of the different parts of the Helix Nebula varies. The temperature of rotational and vibrational motion ranges from 1800 K in a cometary knot located in the inner area of the nebula, about 2.5’ arcminutes away from the central star to around 900 K in the outer region, approximately 5.6’ arcminutes away from the central star [21]. The infrared image of the Helix Nebula taken by the Spitzer Space Telescope is shown in Figure 2.1.

Figure 2.1: Helix Nebula taken by the Spitzer Space Telescope (Infrared, 2007) [22].

Most of the earlier research on the Helix has been on the structure, content, and mobility of the so-called ”cometary knots,” which are dense globules found throughout the Helix’s envelope. Similarly, the dust characteristics, shape, and composition of the helix nebula are being investigated. Some of the pieces are seen below. In a study conducted by Meaburn et al. (1996), the overall expansion velocity of the cometary knots in the Helix planetary nebula (NGC 7293) was found to be 10 km/s, which is lower than the general expansion velocity of the Helix nebula, which is 24 km/s. To determine the

position of each knot, the researchers used [0 III] 5007 Å pictures of the entire Helix nebula. They proposed that the cometary knots were remnants of condensations in the precursor, slower, dense wind formed after the creation of the planetary nebula, which was likely a red giant/AGB star [23].

In their study on the Helix Nebula's cometary knots, Capriotti and Kendall (2006) proposed that the nebula was formed from larger "parent clouds" that fragmented due to Rayleigh-Taylor instability caused by the clouds' radiative acceleration. They calculated various properties of both the cometary knots and the parent clouds, including their locations, velocities, and sizes. The researchers also found that the need for stable cometary knots imposed additional constraints on the characteristics of the parent clouds [20].

Meaburn et al. (1992) conducted a study on the dust in the neutral globules of the Helix Nebula, NGC 7293, and found that the total mass in one globule is at least 1.0×10^{-5} $M_{\odot}$ and the mean mass density N_H is $6.2 \times 10^5 cm^{-3}$ by assuming typical interstellar dust mass ratios and reddening laws. They also observed that the globules and tails must contain dust since they appear contrasting to the diffuse, central [O III]-the emitting volume of the Helix Nebula [24].

In their study published in 2015, Steene et al. investigated the dust in the Helix Nebula (NGC 7293) using Herschel imaging. They found that the total dust mass in the Helix Nebula, excluding the halo, is 3.5×10^{-3} $M_{\odot}$ at a distance of 216 pc. By analyzing the spectral energy distribution of the primary nebula using Herschel, IRAS, and Planck flux measurements, they determined that the dust is mostly composed of amorphous carbon with an emissivity index of $\beta = 0.99 \pm 0.09$, indicating a carbon-rich molecular chemistry. The study also revealed that the dust distribution is clumpy and concentrated in the barrel wall, while a dust excess emission was observed from the core star disk of 70 μm, with dust temperatures ranging from 22 K to 42 K. The researchers concluded that the various emission components are consistent with the Helix, which is composed of a thick-walled barrel-like structure inclined to the line of sight, and that the radiation field rapidly decreases through the barrel wall [25].

Henry et al. (1999) conducted an analysis of the morphology and composition of the Helix nebula. They found that the core star has an effective temperature of 120,000 K and a luminosity of 100 $L_{\odot}$. Additionally, they calculated a lower limit for the nebular mass to be 0.30 $M_{\odot}$. They also determined the following elemental properties of the Helix

nebula: He/H = 0.12 (±0.017), C/O = 0.87 (±0.12), N/O = 0.54 (±0.14), O/H = 4.60×10^{-4} (±0.18), Ne/O = 0.33 (±0.04), Ar/O = 6.74×10^{-3}, and S/O = 3.22×10^{-3} (±0.26) [15].

2.4 Basic Parameter For This Work

The distance to the Helix Nebula is not well determined; it is certainly at the outer limits of accurate parallax measurements. A distance determination based on the Shklovsky method, which assumes the ionized mass and electron temperature are the same for all planetary nebulae, yields a distance of 110 pc [26]. The ionizing flux of the central star of a planetary nebula can change by several orders of magnitude over the life of the nebula indicating that the ionized mass can change. Daub assumed the ionized mass is related to observable radio and infrared quantities and found a distance of 150 pc [27]. Zhang took core mass, luminosity, and surface gravity found by distance-independent quantities and determined a distance of 160 pc [28]. I have taken the distance to the Helix Nebula to be 200 pc in this paper which was taken from Speck et al.(2002) [29]. The central star's coordinates (J2000) are 22:29:38.4 and -20:50:11.4. Other parameters which are used in our dust modeling are given in section 3.

2.5 Dust colour Temperature

An overview of the historical development of the techniques for estimating the dust color temperature will be covered in this section. The analogous temperature of the dust in this context is referred to as the dust color temperature (or wavelength). Infrared Astronomical Satellite (IRAS) and CO data for the black cloud Bernard 5(B5) were presented by Beichmanand his friends in 1988 [30]. They discovered that the 100 μm emission shows the column density of the dust and gas through the cloud. The anti-correlation between molecular line emission and the emission at 12 μm is found to be quite pronounced in the B5 cloud. Small granules, perhaps polyaromatic hydrocarbons (PAHs), which are temporarily heated by the absorption of vigorous UV photons in a thin shell around them, are the source of the short-wavelength emission.

The results from the 60 and 100 μm wavelengths and the 12 and 25 μm wavelengths reveal the following grain color temperatures seen approaching B5: 25-28 K and 300-350 K,

respectively. The grain temperatures seen in B5 at 60 and 100 μm are comparable to or somewhat greater than those predicted for large graphite grains in equilibrium with the Interstellar Radiation Field (ISRF) [30]. It is impossible to comprehend the existence of emission at distances of 12 and 25 μm from the cloud in terms of emission from typical interstellar grains. According to a theory put forth by Puget and his associate [31], the emission from the tiny, stochastically heated grains predominates at shorter wavelengths and may even boost the grains' 60 μm emission.

By noting that for optically thin emission from grains at a single equilibrium temperature, the ratio of the 60 to 100 μm intensity was employed as a measure of grain temperature [32].

The following presumptions were made by Wood and his mate in order to arrive at the formula for the dust color temperature [33].

- At 100 and 60 μm (τ_d <<1), the dust is optically thin. The interstellar extinction curve can provide evidence for this (Figure 1.2).
- The dust emissivity is inversely correlated with a power law ($\tau_d \propto \lambda^{-\beta}$) with index $\beta = 1$. The Planck theory of blackbody radiation clearly supports this supposition.
- The 60 μm and 100 μm beams subtend the same solid angle $\Omega_{60\mu m} \equiv \Omega_{100\mu m}$. This is due to the transition between rotational and vibrational energy levels
- The temperature of the dust in the IRAS beam is constant. It indicates that they are locally in thermal equilibrium.
- Zodiacal light can be eliminated from an image by removing a linear gradient from it.

By assuming that the observed ratio of 60 μm to 100 μm (60 μm/100 μm) emissions are caused by blackbody radiation from dust grains at temperature T_d, adjusted by a power-law emissivity, the 60 μm and 100 μm dust temperature, T_d at each pixel in an image, was estimated. The typical assumption is that the flux recorded by IRAS is the product of the sum of the relevant Planck functions times the opacities.

Langer and his colleague [32] examined the infrared and CO from Bernard 5 (B5) to look into the relationship between dust column density, CO isotope intensities, and visual extinction. They employed a spectral index emissivity $\beta = 1$

Think about a source with a single temperature. In the far infrared, the opacity changes with wavelength and has the form ($\tau_d \propto \lambda^{-\beta}$), where β = 1[34]. The flux density of emission at a wavelength λ_i is given by;

$$F_i = \left[\frac{2\mathrm{hc}}{\lambda_i^3(exp(\frac{\mathrm{hc}}{\lambda_i \mathrm{k} T_d}) - 1)}\right]\tau_i \Omega_i \tag{2.1}$$

With,

$$\tau_i = N_d \alpha \lambda_i^{-\beta} \tag{2.2}$$

where

N_d is the column density of dust grains, α is a constant which relates the flux with the optical depth of the dust, β is the spectral emissivity index, and Ω_i is the solid angle subtended at λ_i by the detector.

Using equation (2.2) in equation (2.1) we get,

$$F_i = \left[\frac{2\mathrm{hc}}{\lambda_i^3(exp(\frac{\mathrm{hc}}{\lambda_i \mathrm{k} T_d}) - 1)}\right] N_d \alpha \lambda_i^{-\beta} \Omega_i \tag{2.3}$$

From above assumption we have τ_d <<1 and $\Omega_{60\mu m} = \Omega_{100\mu m}$. Also, $T_{100} = \frac{hc}{\lambda_{100} k}$ and putting $T_{60} = \frac{hc}{\lambda_{60} k}$, where c is the speed of light, k is the Boltzmann's constant, and h is the Planck constant. Consequently, the ratio R, between the flux densities at 60 μm and 100 μm will be.

$$R = \frac{F_{60}}{F_{100}} = \frac{60}{100}^{-(3+\beta)} \left[\frac{exp\frac{T_{100}}{T_d} - 1}{exp\frac{T_{60}}{T_d} - 1}\right] \frac{\Omega_{60}}{\Omega_{100}} \tag{2.4}$$

From, T_{100} = 144 and T_{60} = 240, then above equation becomes,

$$R = 0.6^{-(3+\beta)} \left[\frac{exp\frac{144}{T_d} - 1}{exp\frac{240}{T_d} - 1}\right] \tag{2.5}$$

Following Dupac et al. (2003) [35]. we use the equation

$$\beta = \frac{1}{\delta + \omega T_d} \tag{2.6}$$

To describe the observed inverse relationship between temperature and emissivity spectral index. Where δ and ω are fee parameters of dimensionless and temperature-inverse

dimension respectively. Dupac et al. (2003) discovered that the hyperbolic approximation function closely approximates the temperature dependency of the emissivity spectral index. The value of β relies on the composition, size, and compactness of the dust grains. A pure black body would have a value of $\beta = 0$, the amorphous layer-lattice material would have a value of $\beta \sim 1$, and metals and crystal clear dielectrics would have a value of $\beta \sim 2$. In the cloud of interest, at the dust temperature, $\frac{T_i}{T_d} >> 1$, due to this, the number one is removed from the equation's (2.5) denominator and numerator, so the equation (2.5) becomes

$$R = 0.6^{-(3+\beta)} \left[\frac{exp\frac{144}{T_d}}{exp\frac{240}{T_d}} \right] \tag{2.7}$$

Natural logarithms on both sides allow us to determine the temperature expression as;

$$T_d = \frac{-96}{ln\{R \times 0.6^{(3+\beta)}\}} \tag{2.8}$$

where R is given by

$$R = \frac{F(60\mu m)}{F(100\mu m)} \tag{2.9}$$

The flux densities at 60 μm and 100 μm, respectively are F(60 μm) and F(100 μm). Using the flux densities at 90 μm and 140 μm and the Dupac et al. (2003) approach used in the IRAS survey, the formula for dust color temperature for the AKARI Survey becomes

$$T_d = \frac{-57}{ln\{R \times 0.64^{(3+\beta)}\}} \tag{2.10}$$

where R is given by

$$R = \frac{F(90\mu m)}{F(140\mu m)} \tag{2.11}$$

Similarly, for the WISE survey at 12 μm and 22 μm the dust color temperature is given by

$$T_d = \frac{-546}{ln\{R \times 0.54^{(3+\beta)}\}} \tag{2.12}$$

where R is given by

$$R = \frac{F(12\mu m)}{F(22\mu m)} \tag{2.13}$$

In this way, we can use equations (2.8), (2.10), and (2.12) for the determination of the dust grain temperature.

2.6 Dust Mass

Hildebrand et al (1977) [36], provide the flux density at frequency ν from an optically thin cloud at a distance D that contains N numbers of spherical dust grains with a radius of a and a temperature of T is

$$F(v) = NB(v,T)Q(v)\frac{\pi a^2}{D^2} \tag{2.14}$$

Here, Q(v) represents the emissivity of dust grains, and B(ν,t) is the Planck function. In a cloud, the volume of dust is given by,

$$V = Nv \tag{2.15}$$

Where v represents the individual grain volume. Solving equations (2.14) and (2.15) we get,

$$V = \frac{\frac{v}{\pi a^2}}{Q_v}\left[\frac{F_v D^2}{B(\nu,T)}\right] \tag{2.16}$$

The estimated dust masses are determined by the IR flux densities, and the calculated dust mass is influenced by the physical and chemical characteristics of the dust particles, the chosen dust temperature T, and the distance D from the object. and hence dust mass having grain density, ρ is,

$$M_{dust} = \frac{4\alpha\rho}{3Q_v}\left[\frac{F_v D^2}{B(\nu,T)}\right] \tag{2.17}$$

where

α = weighted grain size

ρ= grain density

D = Distance to the star

Q_v = grain emissivity

Young et al. (1993) [37] determined the following values for the grain for the emitter at 100 μm: grain size (a) = 0.1 μm, grain density (ρ) = 3000 Kg m^{-3}, grain emissivity for the emitter at 100 μm (Q_v)= 0.0010, and grain emissivity for the emitter at 60 μm (Q_v) = 0.0046.

According to Beichman et al. (1988) [38], the relative flux density values obtained from the IRAS picture (f) may be translated into absolute values as follows:

Flux density (F_ν) = f × MJy/sr× 5. 288 × 10^{-9}

Here, 1 MJy/sr = 1 ×10^{-20} kg s^{-2}. Then equation (2.17) becomes

$$M_{dust} = 0.40\left[\frac{F_\nu D^2}{B(\nu, T)}\right] \tag{2.18}$$

Here, Planck's function, which is denoted by the following equation, is a well-known function.

$$B(\nu, T) = \frac{2\mathrm{h}\nu^3}{\mathrm{c}^2}\left[\frac{1}{exp(\frac{\mathrm{h}\nu}{\mathrm{k}T}) - 1}\right] \tag{2.19}$$

Where,

h = Planck's constant

c = velocity of light

ν = The frequency at which the emission is seen

T = Temperature of each pixel

The physical and chemical characteristics of the dust particles, the temperature of the dust, and the distance from the item all affect the mass of dust present.

The formula given in equation (2.19) makes it evident that the value of the Planck function B (ν, T) for longer wavelengths is greater than that for shorter wavelengths. As a result, the range of B (ν, T) for fixed temperature (Let's say δ T) goes narrower if the wavelength of the images increases.

Relation of mass of the gas to dust mass

It was supposed that the optical extinction ratio, A_ν, to Hydrogen column density is the same as that for the intercloud medium, and that their ratio, as well as the ratio $\frac{A_\nu}{\tau_\nu}$ for the calibration object, may be applied to denser clouds. Here, τ_ν represents the sub-millimeter optical depth. Here we introduce a gas mass to dust ratio $\frac{M_g}{M_d}$, ($M_g \equiv M_{cloud}$), then we can write the equation (2.17),

$$M_c = \frac{4\alpha\rho}{3Q_\nu}\left[\frac{F_\nu D^2}{B(\nu, T)}\right]\frac{M_g}{M_d} \tag{2.20}$$

Theoretically, a value for $\frac{M_g}{M_d}$ may be obtained from observations of dust volume and hydrogen column density. In this case, the entire factor of equation (2.18) is estimated using measurements of the flux density, temperature, and extinction. Hildebrand (1983) discovered the ratio $\frac{M_g}{M_d} = \frac{10}{0.1} = 100$

Following the calculations of Young et al. (1993) [37], To estimate the dust masses using

the infrared flux densities at 100 μm, we must convert the background-adjusted value of the infrared flux density to the absolute flux density. The background adjustment involves subtracting the average flux emitted by other sources besides the object under study. The physical and chemical properties of the dust grains are the factors that determine the final dust mass.

2.7 The Jeans Limit

A gas cloud that is roughly in the starting stage of its collapse due to its own gravitation is described. When the mass of a cloud is high enough, the potential energy of the cloud can exceed its kinetic energy, leading to cloud collapse. The virial theorem dictates that the potential energy must be at least twice the kinetic energy for collapse to occur. This criterion establishes the critical mass and length required for cloud collapse. Sir James Jeans first proposed this standard in 1902 [3]. According to the viral theorem, the condition for stability is,

$$< T > + \frac{1}{2} < U >= 0 \tag{2.21}$$

The molecular cloud will be bounded or compressed due to gravity only if

$$< T > + \frac{1}{2} < U > \quad < 0 \tag{2.22}$$

The gravitational potential energy is given by,

$$< U >= \int_{0,r=0}^{M,r=R} -\frac{\mathrm{Gm}}{r} dm = -\frac{\mathrm{GM}^2}{2R} \tag{2.23}$$

Similarly, the kinetic energy of non-degenerate gas is given by,

$$K.E = \frac{3\mathrm{Mk}T}{2\mu \mathrm{m_H}} \tag{2.24}$$

Here, μ is the molecular weight, and its value is given by,

$$\mu = \frac{1}{\alpha X + \beta Y + \gamma Z} \tag{2.25}$$

The value of the α, β and γ for the completely ionized gas are, $\frac{2}{1}$, $\frac{3}{4}$ and $\frac{1}{2}$ respectively. Similarly, X, Y, and Z are the percentages of hydrogen, helium, and other heavy elements. Using equations (2.23) and (2.24) in equation (2.22) we get,

$$\frac{3\mathrm{Mk}T}{2\mu \mathrm{m_H}} - \frac{1}{2}\frac{\mathrm{GM}^2}{2R} < 0 \tag{2.26}$$

$$M > 6\frac{\mathrm{k}T}{\mu \mathrm{m_H G}}R \quad \text{Jeans Mass } \mathrm{M_J} \tag{2.27}$$

The total mass of the cloud should be greater than M_J in order to collapse the molecular cloud of non-degenerate gases gravitationally. Here R is the radius of the cloud which is spherically in shape. For a spherical cloud, the density is,

$$\rho = \frac{M}{V} = \frac{M}{\frac{4}{3}\pi R^3} \tag{2.28}$$

$$>>> R = \left[\frac{3M}{4\pi\rho}\right]^{\frac{1}{3}} \tag{2.29}$$

Substituting (2.29) in (2.27) we get,

$$M > 6\frac{\mathrm{k}T}{\mu \mathrm{m_H G}}\left[\frac{3M}{4\pi\rho}\right]^{\frac{1}{3}} \tag{2.30}$$

Solving this we get,

$$M > \left\{6\frac{\mathrm{kT}}{\mu \mathrm{m_H G}}\right\}^{\frac{3}{2}}\left\{\frac{3}{4\pi\rho}\right\}^{\frac{1}{2}} \tag{2.31}$$

This expression is called jeans mass M_J. For Jeans length substitute Jeans mass in equation (2.29)

$$R = \left[\frac{3M_J}{4\pi\rho}\right]^{\frac{1}{3}}$$

$$>>> \lambda_J = \left[\frac{3}{4\pi\rho}\right]^{\frac{1}{3}}\left[\left\{6\frac{\mathrm{kT}}{\mu \mathrm{m_H G}}\right\}^{\frac{3}{2}}\left\{\frac{3}{4\pi\rho}\right\}^{\frac{1}{2}}\right]^{\frac{1}{3}} \tag{2.32}$$

Simplifying we get,

$$\lambda_j = \left[\frac{9\mathrm{k}T}{2\pi\mu \mathrm{m_H G}\rho}\right]^{\frac{1}{2}} \tag{2.33}$$

Which is the required expression for the Jeans Length. In order to have gravitational collapse M ¿ M_J and λ ¡ λ_J

The Jeans length is the oscillation of wavelength below which stable collection rather than gravitational collapse will occur. At this critical length, the cloud neither expands nor contracts.

2.8 The Density Distribution Function

This axisymmetric density distribution function is based on the premise that mass loss during the AGB phase is spherically symmetric and changes to axisymmetric during the subsequent "superwind" phase. Using this function, a three-layer density distribution is defined. Due to the early AGB mass loss occurring in nearly perfect spherical symmetry, the outermost area possesses a spherically symmetric, power-law density distribution $\rho(R, \theta) \propto R^{-B}$. The density distribution is axisymmetric and shows an equatorial enhancement in the innermost region. It is believed that the axisymmetric superwind towards the end of the AGB phase is what generated the equatorial boost. In section 3, we get more information about this function.

2.9 Surveys

Here, we provide a brief overview of the goals, equipment, and lighting of the three all-sky surveys whose data we used for this investigation. These are IRIS, WISE, and AKARI.

2.9.1 Improved Reprocessing of the IRAS Survey(IRIS)

The IRIS (for Improved Reprocessing of the IRAS Survey) results from this new generation of IRAS maps will be of special relevance to the Planck mission, which is dedicated to studying the cosmic microwave background (CMB) [39]. IRIS is the new generation of IRAS maps so, let's discuss IRAS.

Infrared Astronomical Satellite (IRAS)

Understanding solar system components and star-forming regions has benefited greatly from infrared data. It assists us in identifying galaxies with significant bursts of newly produced stars, revealing astronomical sources hidden by interstellar dust, and defining the emission process seen in active galactic nuclei.

Due to the Earth's atmosphere's obscuration, thermal radiation from warm telescopes, and the atmosphere, it is challenging to conduct unbiased and sensitive all-sky surveys at infrared wavelengths. By undertaking an all-sky survey from a satellite using a cooled telescope, the Infrared Astronomical Satellite (IRAS) mission was created to get around these challenges. The Infrared Astronomical Satellite (IRAS), seen in Figure 2.2 (a), (b),

scanned over 96% of the sky at wavelengths between 10 and 100 μm with a sensitivity that was as close as was practicable to the upper limit imposed by variations in the thermal emission from the zodiacal background. This survey's point source catalog is meant to be extremely trustworthy (¿ 99.8%) [40].

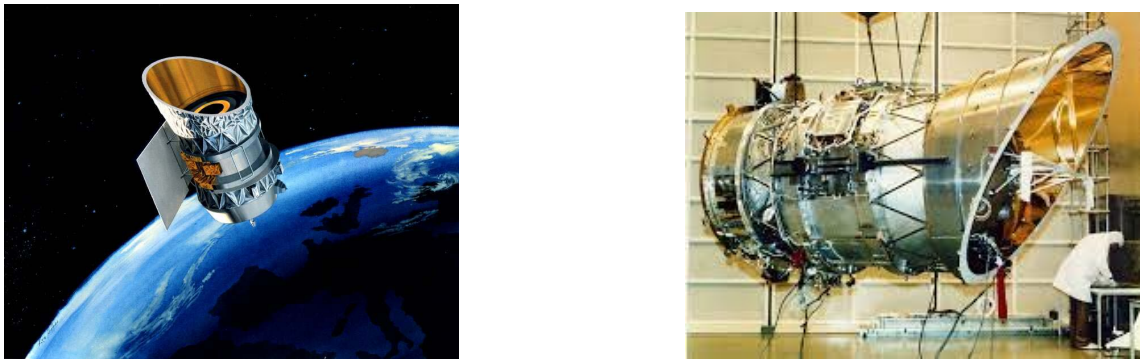

(a) **(b)**

Figure 2.2: (a) IRAS -Universe mission [41]. (b)IRAS during the magnetic moment test conducted in the Netherlands. The satellite was slowly spun and the variations in the magnetic field were measured [42].

The US, UK, and Netherlands all worked together on the IRAS project. At 12, 25, 60, and 100 μm, the IRAS mission carried out an objective, sensitive all-sky survey. The survey plan and satellite architecture were designed for the most accurate point source detection possible. Along with the survey observations, pointed observations, usually referred to as Additional Observations or AOs, were made. By doubling the number of astronomical sources that are now known, this ground-breaking infrared satellite significantly advanced science. Six new comets, very intense infrared emission from colliding galaxies, and wisps of warm dust known as infrared cirrus that could be discovered in practically every direction of space were among the findings made by IRAS. The Milky Way's core was also made known by IRAS for the first time. Nearly two decades after this significant trip, archival research using IRAS data is still being conducted. 96% of the sky was examined by the Infrared Astronomical Satellite (IRAS) between January and November 1983. The four wavelength bands used for the IRAS survey had their centers at 12, 25, 60, and 100 μm. It spent around two-thirds of its 300-day mission conducting an impartial survey of the sky, which resulted in the publication of the IRAS Point Source Catalog (PSC) in 1984, which comprises about 250,000 sources. More than half of the sky was covered by more than twelve separate detector scans per wavelength band when

IRAS repeatedly scanned the sky with numerous detectors. Astronomers started thinking about the potential of mounting an infrared telescope on a satellite in Earth orbit in the 1970s. Because it would be located above the atmosphere of the Earth, this telescope would be able to see wavelengths of the infrared spectrum that are invisible to the human eye. It has the capacity to take in a lot of sky and keep an eye on specific areas for a while. By 1977, the Netherlands, the United States, and Great Britain had established an international partnership to create IRAS. The telescope, detectors, and cooling system were created by an American team. The Dutch team developed the spacecraft, which featured the onboard computers and pointing equipment, while the British team created the satellite ground station and control center. The entire telescope was chilled to just a few degrees above absolute zero because, if not, it would generate infrared radiation that would obstruct the observations. A space infrared telescope needs to be colder than the things it will be looking at in space. Six new comets, very intense infrared emission from colliding galaxies, and wisps of warm dust known as infrared cirrus that could be discovered in practically every direction of space were among the findings made by IRAS. The Milky Way, the center of our galaxy, was also made public by IRAS for the first time [40].

The IRAS satellite includes a spacecraft and a liquid helium cryostat enclosing a cooled telescope. The telescope is an f/9.6 Ritchey-Chretien design with a 5.5 m focal length, 0.57 m aperture, and beryllium mirrors chilled to less than 10 K. The system's response to off-axis radiation is decreased via a series of internal cold baffles. The sun and earth's heat load are minimized on the cold optical system by external baffles and the sunshade (at $\sim$ 100 K). The total flux at the focal plain from all brilliant sources of off-axis emission during a normal survey is less than a small percentage of the thermal emission of the zodiacal dust particles for the range of observing angles utilized [43]. Figure 2.3 depicts schematically the focal plane assembly, which is situated at the telescope's Cassegrain focus and is cooled to a temperature of less than 3 K. The survey array's sixty-two infrared detectors are placed so that at least two detectors in each of the four wavelength bands may see every source that crosses the field of view. Spectral filters and field lenses come before each detector. Since the electronics are directly connected, it is possible to measure the entire flux passing through the telescope. The 7.5 to 23 μm wavelength range of the low-resolution spectrometer (LRS), a slitless spectrometer. For all suitably bright point

sources that traverse the LRS aperture, spectra with a resolution of about 20 are generated from the data stream based on timing obtained from the survey array.

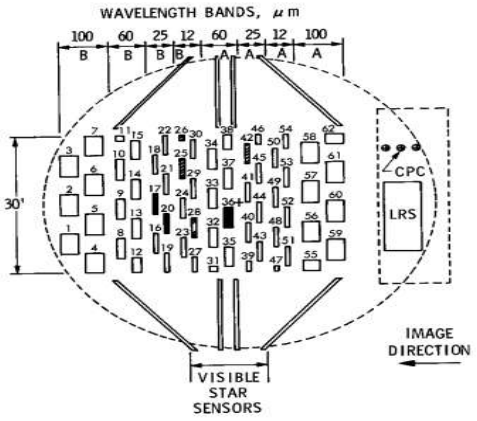

Figure 2.3: The IRAS focus plane is illustrated schematically. The rectangles in the center indicate a survey array detector, filter, and field lens combination. The image of the source appears in the focus plane in the direction specified. The shaded detectors are either inoperable or substantially so; these abnormalities were recognized before to launch [44].

Infrared sources are mapped simultaneously at 50 and 100μm with improved spatial resolution via the chopped photometric channel (CPC), which is active during certain directed observations. Since the CPC includes an internally cooled chopper, signal modification by scanning is not necessary, and it also offers an absolute flux reference [45]. On January 26, 1983, GMT, the satellite was sent into a 900 km high, almost polar orbit. The supply of cryogenic helium ran out on November 22, 1983, around 05:00 GMT. The orbit precesses so that it stays close to the terminator's plane and has an inclination of 99 degrees with regard to the equator of the planet. By rotating the entire satellite, the telescope could be pointed up to 30 degrees away from the local vertical. Rotating around the satellite's direction to the Sun at fixed solar elongation angles between 60 and 120 degrees allowed for sky scans. The boresight scanned the sky in survey scans at a speed of 3.85 cents per minute.

2.9.2 AKARI

The Japan Aerospace Exploration Agency (JAXAM-V-8)'s rocket carried the AKARI Satellite into orbit from Uchinoura Space Center on February 21, 2006 (UT) (USC).

After it was confirmed that the satellite had been successfully launched into orbit, it was given the new name AKARI. The Japanese space mission AKARI is the successor to the Infrared Telescope in Space (IRTS) on board the Space Flyer Unit(SFU) [46]. As an infrared All-Sky Survey mission, AKARI is projected. The project's main goal is to deliver second-generation infrared catalogs with greater geographical resolution and spectral coverage than the first catalogs produced by the Infra-Red Astronomy Satellite (IRAS) mission [40]. AKARI is fitted with a 68.5cm aperture diameter cryogenically cooled telescope and two pieces of scientific equipment, the Far-Infrared Surveyor (FIS) Kawada et al. (2007) [47] and the Infrared Camera (IRC) Onaka et al. (2007) [48]. The broad fields of view covered by these devices' large-format arrays make them ideal for effective surveys. In addition to the All-Sky Survey, AKARI can perform precise observations. A high-efficiency liquid-Helium cryostat with a long cryogenic duration and a modest volume of liquid Helium was particularly built for AKARI [49].

The AKARI satellite, a specialized space probe for infrared astronomical studies, was used to observe the entire sky. The telescope's two focal-plane instruments (FPIs), the InfraRed Camera and the Far-Infrared Surveyor allowed it to observe over the 2-180 μm near-infrared (NIR) to FIR spectral ranges. Instrumental thermal emission was decreased by cooling both FPIs and the telescope to 6 K with the aid of mechanical double-stage Stirling coolers and liquid helium cryogen [49]. The satellite was put into a Sun-synchronous polar orbit, which had an orbital period of 98 minutes, an inclination angle of 98.2 degrees, and an altitude of 700 km. This orbit allowed the satellite to travel down the Earth's equator during the day and at night. The telescope's pointing was kept orthogonal to the Sun-Earth direction and away from the Earth's center during the survey observations. As a result, the spacecraft received minimal radiation from the Earth and steady radiation from the Sun [46]. The AKARI telescope continually scanned the sky along the great circle with a constant scan speed of 3.6'$s^{-}1$ while in this orbital configuration. The Earth's yearly rotation causes a ∼4' shift in the scan direction each satellite revolution, either longitudinally or cross-scan. As a result, during each six-month period of continuous observation, the entire sky may be surveyed.

The FIS instrument, which was intended for photometric scanning and spectroscopic also displayed for comparison, was used to undertake the all-sky survey observations at FIR wavelengths. Spectral observations from the 50-180 μm range in color. The all-sky survey

employed four photometric bands. The WIDE-S band (50-110 μm, centered at 90 μm) and the WIDE-L band (110-180 μm, centered at 140 μm) were two of the four bands with the broadest wavelength coverage and continuous coverage of the whole waveband range. The N60 band (50-80 μm, centered at 65 μm) and the N160 band (140-180 μm, centered at 160 μm) are the two additional bands that sampled both the shorter and longer ends of the wavebands and had narrower wavelength coverage. The detectors' pixels were 26".8 $\times$ 26".8, for the bands with short wavelengths (N60 and WIDE-S), and 44".2$\times$ 44".2 for the bands with large wavelengths N60 and WIDE-S had a cross-scan width of 8 while WIDE-L and N160 had a cross-scan width of 12. Two or three times the shift in the scan direction per satellite revolution was represented by these array sizes [47].

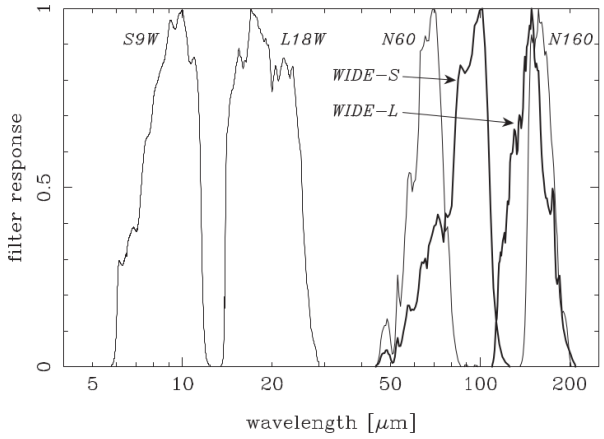

Figure 2.4: For the two AKARI/IRC bands (S9W and L18W) and the four AKARI/FIS bands (N60, WIDE-S, WIDE-L, and N160), the relative spectral response function (RSRF) was plotted versus the energy flow. The maximum values of the RSRFs were used to normalize them [50].

As a consequence of a continuous survey observation, the N60, WIDE-S, and N160 bands were used to survey regions near the ecliptic plane at least twice each, while the WIDE-L and WIDE-S bands were used three times each. We utilized the WIDE-S and WIDE-L databases for two of our infrared cavities. pictures of the entire sky taken during the AKARI FIR survey in wavelengths of 65 μm, 90 μm, 140 μm, and 160 μm.
The high spatial resolution from 1' to 1.5' of the AKARI FIR survey displays the large-scale distribution of ISM with excellent detail in addition to the ¿99% coverage of the whole sky. The IRC offers fluxes in the S9W and L18W photometric bands, whose respective center wavelengths (λ_c) are 9 and 18 μm. The four photometric bands N60, WIDE-S,

WIDE-L, and N160, with center wavelengths of 65, 90, 140, and 160 μm, respectively, are supplied by the FIS. Figure 2.4 displays the relative spectral response functions (RSRFs) for the six bands.

2.9.3 The Wide-Field Infrared Survey Explorer (WISE)

By mid-July 2010, the Wide-field Infrared Survey Explorer (WISE), which has significantly higher sensitivity than earlier infrared scan missions, will have finished a mid-infrared survey of the whole sky. A 40 cm telescope feeding array with a total of 4 million pixels is being used by WISE to map the whole sky in four infrared bands, W1..W4, with focal lengths of 3.4, 4.6, 12 & 22 μm. As a result of the larger number of detectors, WISE's sensitivity in the 12 μm band is greater than a hundred times that of IRAS. While IRAS had two far-infrared bands at 60 and 100 μm, WISE had two mid-infrared bands at 3.4 and 4.6 μm. The Diffuse InfraRed Background Experiment (DIRBE) on the COBE satellite is the only all-sky survey that has been performed in these bands, and DIRBE used just one pixel per band to observe a 0.7° beam. Smith et al. (2004) [51] created a point source catalog using the DIRBE data, with flux limitations of 60 & 50 Jy at 3.5 & 4.9 μm. WISE should be able to achieve flux limits that are 5×10^4 times lower in these bands.

WISE is a NASA MIDEX (mid-class Explorer) project. For the principal investigator, Edward L. Wright, the project is overseen and operated by the Jet Propulsion Laboratory (JPL). Contractors constructed the instrument and spacecraft, respectively, Utah State University's Space Dynamics Laboratory (SDL) and Ball Aerospace & Technologies Corporation partnered. The data is examined and processed by the Infrared Processing and Analysis Center (IPAC). The UC Berkeley Space Sciences Lab is in charge of organizing WISE's educational and public outreach initiatives (Mendez 2008) [52]. The WISE flight system measures 285 cm in height, 200 cm in width, and 173 cm in depth. It weighs 661 kg. It consumes 301 W of power, although the solar panels are capable of producing over 500 W. A solid-hydrogen-cooled cryostat houses a 40 cm diameter telescope. At launch, the solid hydrogen weighs 15.7 kg while the cryostat, telescope, and camera together weigh 347 kg. The operational configuration of the flight system is depicted in Figure 2.5

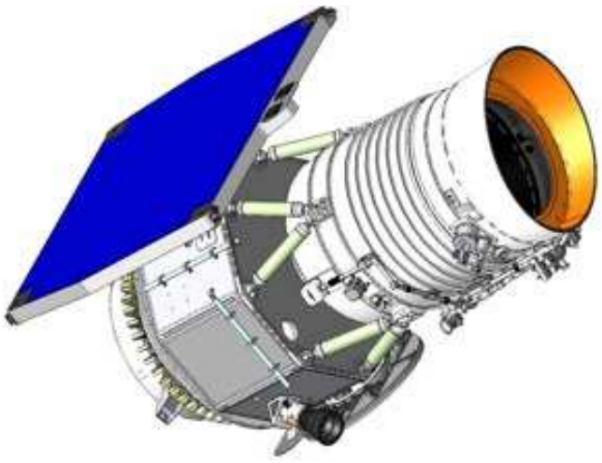

Figure 2.5: Diagram depicting the WISE flying system in survey mode with the cover removed. The spacecraft bus to the left of the bipod supports was given by BATC, while the cryogenic instrument to the right of the bipods was provided by SDL [53].

L-3 Communications SSG-Tinsley was responsible for designing and building the optics for the WISE telescope and camera. A 40 cm diameter afocal telescope generates a beam of light that travels in parallel and is directed into the scan mirror. The scan mirror also operates in the parallel beam before the light enters the all-reflecting camera. Before the scan mirror, the afocal telescope has six mirrors, including foldable flats. After the scan mirror, the camera has six mirrors. A high infrared transmission is provided by the gold coating on all of the mirrors. More information on the design is provided by Wright, E. L. (2009) [54].

WISE creates excellent maps of interstellar dust in the Galaxy and can detect the majority of its components. The continuum emission from extremely small grains is measured by the 4.6 μm filter, which also includes significant PAH emission features. The 22 μm filter observes stochastic emission from small grains as well as the Wien tail of thermal emission from large grains. With a sensitivity 60 times higher at 22 μm and 200 times higher at 12 μm than IRAS, the WISE survey will map the high-latitude dust. The 3.4 μm map will give a signal-to-noise ratio equal in sensitivity to the 12 μm map for typical high latitude dust exhibiting PAH emission. The mapping of high latitudes is thus expanded by the WISE survey. The first high-sensitivity map of extended emission of the entire sky at this wavelength will be provided by the 3.4 μm map. These expanded emission maps will make it possible to investigate the structure and chemical makeup of interstellar dust. It is possible to determine the composition of PAHs by contrasting the WISE-specific 3.3 μm

PAH signature with other PAH emission characteristics in diffuse clouds. The findings of the study of galaxy dust can also be contrasted with dust emission found by WISE in adjacent galaxies.

2.10 Motivations

We were inspired by Steene et al. (2015) [25] to complete this work for the following reasons:

1. Nebulae in ISM is the birth and death place of the star so, the study of the nebulae has become one of the most dynamic areas of astrophysical research, as the ways in which they are involved with the lives of stars have become clearer.

2. A comprehensive all-sky database at 12, 25, 60, and 100 μm wavelengths is offered by the Infrared Astronomical Satellite Survey (IRAS). The SkyView virtual observatory's IRIS virtual observatory also offers IRAS-processed and calibrated data. A recent database at 90 and 140 μm wavelengths has been provided by AKARI, a Japanese satellite with the designation "light." For studying interstellar dust, these wavelengths are quite helpful. Similarly, WISE produces superior interstellar dust maps and can identify the bulk of its constituent parts. In the current investigation, we want to use data from the 60 and 100 μm IRAS, the 90 and 140 μm AKARI, and WISE 12 and 22 μm telescopes of a few chosen regions where the nebula and dust can both be seen.

3. We want to examine the dust temperature distribution and determine whether or not it is Gaussian. We also want to create a dust color temperature map of the area of interest. This map will show information about the hot and cold regions.

4. The dust mass distribution may or may not match the distribution of dust color temperature. Our goal is to create dust mass maps of whole nebulae and contrast them with a map of dust color temperature.

2.11 Objectives

The main objectives of the work will be to study dust properties around the helix nebula(NGC-7293) using IRIS, AKARI, WISE Surveys, and the 2-Dust model. Some specific objectivity of the study is given below.

- To calculate the dust color temperature, dust mass distribution, distribution of flux, and Jean's criteria of the nebula will be examined, talked about, and then contrasted.
- To produce and compared the dust color temperature and dust mass maps of the field.
- To determine the mass loss rate, luminosity, inner shell radius, outer shell radius, and other dust properties of helix nebula using density distribution function (2-Dust) and then compare to another model such as simple radiative transfer model and DUSTY model.

Chapter 3

Method and Methodology

This chapter describes the general approach and methods adopted to address the objectives of the study. The chapter also explains the data source and the limitations of the study. It also explains the research design and statistical tools.

We use the color map and Gaussian function modeling for the data available. The distribution of infrared flux, dust color temperature, and dust mass, are all studied by color map plots. The Gaussian modeling is performed for temperature, flux, and mass. We also study the density distribution function.

3.1 Density Distribution Function

We employ the 2-Dust radiative transfer code for our modeling. In section 3.8.1, we'll go into further detail. In these computations, the circumstellar dust shell is axisymmetric and illuminated by the central star, which scatters and reddens the starlight. The requirement for global brightness constancy at each radial grid point in the dust shell results in self-consistency. This study's main focus is the density function of the dust shell since it has a direct bearing on the mass-loss history of the object. A density function that can have a toroidal inner, an elliptical (prolate or oblate) mid-region, and a spherical outside shell is what we've chosen in this case. This function represents the idea that during the superwind phase ($M_{\rm sw}$), the mass-loss rate switched from being spherically symmetric on the AGB ($M_{\rm AGB}$) to being axisymmetric. Following are the density functions that we used in our

work [55]:

$$\rho(R,\theta) = \rho_{\min}\left(\frac{R}{R_{\min}}\right)^{-B}\left\{1+Csin^{F}\theta\left[e^{-(R/R_{sw})^{D}}/e^{-(R_{min}/R_{sw})^{D}}\right]\right\} \times\left\{1+A(1-cos\theta)^{F}\left[e^{-(R/R_{sw})^{E}}/e^{-(R_{min}/R_{sw})^{E}}\right]\right\}, \tag{3.1}$$

$R_{\min} < R < R_{\max}$

Here,

$\rho(R,\theta)$ = The mass density of dust grains at radius R and latitude θ

$\rho_{\min}$ =The density of dust grains on the polar axis near the envelope's inner border.

$R_{\min}$ = The inner radius of the shell

$R_{\max}$ = The outer radius of the shell

$R_{\rm sw}$ = The border between the spherical AGB wind and the axisymmetric superwind.

The first term, $\frac{R}{R_{\min}^{-B}}$, defines the radial profile of the spherical AGB wind.

$[1 + C....]$ a term that follows B in the exponent defines the elliptical mid-shell.

The second term, "[1+A...]," defines the equatorial enhancement of the superwind. The density profile is determined by the user-defined constants A–F. The degree of equatorial enhancement is set by A, where $1 + A$ is the equator-to-pole density ratio at $R_{\min}$, and C, where the density drop with radius along the equator is steepened by a factor of (1+ C). The inner torus can be made torus-like or disk-like with F, while D and E define the mid-shell region as oblate or prolate.

The 2D density function used in the "best" model of the Helix Nebula is also shown in Equation (3.1). Table 3.1 provides a list of user-defined constants for the model density function. The optical depth of the dust shell at the equator at a specific user-set wavelength determines ρ.

Table 3.1: Parameter for 2-dust model

Parameter	Value	Reference
Radius	0.024 $R_\odot$	[56]
Temperature	120000.0 K	[15]
Distance	200 pc	[30]
Expansion velocity	35.0 m/s	[16]
optical depth(τ_{18})	0.12	[57]
A	9	This work
B	2.0	This work
C	1.0	This work
D	3	This work
E	3	This work
F	3	This work

Our modeling also places limitations on the dust particle's characteristics. We assume a power law pulse exponential fall off for the grain-size distribution [56],

$$a^{-3.5}e^{-a/a_0}, a_{\min} < a < \infty, \tag{3.2}$$

This is defined by an effective maximum grain size a_0 and a minimum grain size $a_{\min}$, and for which the number of grains larger than a_0 is decreasingly tiny [58]. This grain-size distribution was created for the interstellar medium (ISM), thus it might or might not work for grains that are found around other stars. Although this parameter has not yet been seen, a theoretical analysis by Dominik, Sedlmayr, and Gail (1989) [59] suggests that the grain-size distribution formed in the circumstellar environs of AGB stars has a steeper power law ($a - 5$). Using the Mie theory and dust optical constants obtained from laboratory tests, the absorption and scattering cross-sections are calculated for each wavelength. We take into account a fiducial grain with size- and composition-averaged cross sections at each wavelength for the radiative transfer [60]. For our source, the dust qualities are listed in Table 3.2.

Parameter	Value	Reference
ρ_{grain}	1.0 gm cm^{-3}	This work
Mass weight	0.5	This work
γ	3.5	[29]
a_{min}	0.005 μm	[29]
a_{max}	0.1 μm	This work
R_{min}	40.0 arcsec	This work
R_{max}	5.5 arcsec	This work
R_{sw}	1.0 arcsec	This work

3.2 Dust Colour Temperature

We use the approach suggested by Draine, B. T., and Lee, H. M. (1984) [34], and Dupac et al. (2003) [35], to calculate the dust color temperature and is given by

$$T_d = \frac{-96}{ln\{R \times 0.6^{(3+\beta)}\}} \tag{3.3}$$

where R is given by

$$R = \frac{F(60\mu m)}{F(100\mu m)} \tag{3.4}$$

The derivation and explanation of equation (3.3) in Chapter 2 (Section 2.5) of the Theory.

3.3 Planck Function

The wavelength (frequency) and, consequently, temperature affects Planck's function's value. The dust mass is then calculated using it. The formula for Planck's function is,

$$B(\nu, T) = \frac{2h\nu^3}{c^2}\left[\frac{1}{exp(\frac{h\nu}{KT}) - 1}\right] \tag{3.5}$$

Where,

h = Planck's constant

c = velocity of light

ν = frequency at which the emission is observed

It is obvious from the expression that longer wavelengths have a higher value for Planck's

function B(ν, T) than shorter wavelengths. Chapter 2 of the literature review provides a discussion of this equation (3.5).

3.4 Dust Mass

We initially calculated the flux density (F_v) at 100 μm maps and used the Hildebrand(1983) [36] formula to calculate the dust mass,

$$M_{dust} = \frac{4\alpha\rho}{3Q_v}\left[\frac{F_v D^2}{B(v,T)}\right] \tag{3.6}$$

The slopes of fitted scatter plots comparing flux densities at 100 μm versus 60 μm are used to determine Planck's function. To determine its dust mass, we use the loops' known separation. In the chapter on the literature review (section 2.6), the expression (3.6) is described in depth.

3.4.1 Jeans Criteria

We use the following formula to calculate the Jeans criteria,

$$M_J = \left\{6\frac{\mathrm{k}T}{\mu \mathrm{m_H G}}\right\}^{\frac{3}{2}}\left\{\frac{3}{4\pi\rho}\right\}^{\frac{1}{2}} \tag{3.7}$$

and

$$\lambda_j = \left[\frac{9\mathrm{k}T}{2\pi\mu \mathrm{m_H G}\rho}\right]^{\frac{1}{2}} \tag{3.8}$$

The derivation and explanation of equations (3.7) and (3.8) in Chapter 2 (Section 2.7) of the Theory.

3.5 Database: Catalog and Selection of Source Nebula

One catalog is used to find this nebula. This catalog was compiled by Acker Agnes et al. (1993) [61]. This catalog is available for all the nebulae, but our focus was on the Helix Nebula (NGC-7293) as no previous studies on 2-Dust modeling had been conducted for this source. We used the SIMBAD database (http://simbad.u-strasbg.fr/simbad/sim-fid) to obtain the coordinates and magnitude of the nebula. Hence, we selected the Helix Nebula as our target for this study.

3.6 Flux and Image Download

We downloaded the required FITS (Flexible Image Transport System) file and image from Sky View Virtual Observatory (http://skyview.gsfc.nasa.gov/current/cgi/titlepage.pl) which contains flux and other information about the source object and it was collected from the IRAS, AKARI, and WISE satellites. The following input parameters are given to download the image and fit the data file from Sky View Virtual Observatory.

Coordinate: J2000 (Galactic coordinates have been used)

Projection: Gnomonic (Gnomonic projection is a non-conformal map projection obtained by projecting points of three-dimensional celestial objects onto the surface of a sphere.)

Image size (pixel): 500 × 500

Image size (degrees): 0.5×0.5 (IRIS), 0.3×0.3 (AKARI), and 0.05×0.05 (WISE)

Brightness Scaling: Logarithmic

Color Table: Stern Special (minimum flux density is represented by dark black and the maximum value of the flux density is signified by white)

Provenance: NASA IPAC/Jet Propulsion Laboratory

Copyright: Public Domain

Some images taken from the sky view virtual observatory using this parameter is shown below.

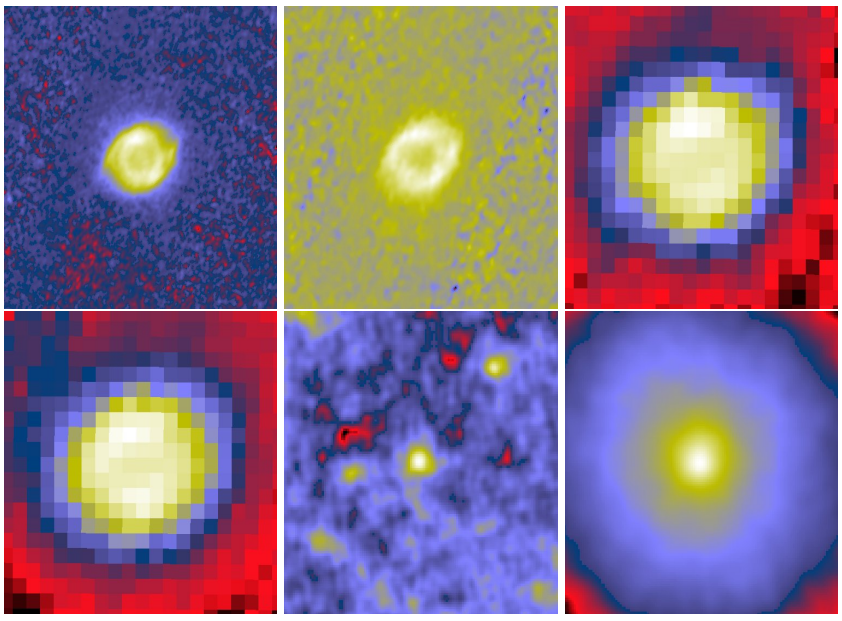

Figure 3.1: JPEG images of Helix for the study in AKARI, IRIS, and WISE.

3.7 Photometric and Far-Infrared Data

The table below displays the photometric and near-infrared data needed for this research project, which was collected from wave sites and different literature.

3.7.1 Photometry Data

Table 3.2: Photometric Data Measuring From Different Missions [62]

.

Missions	**Wavelength (μm)**	**Flux (Jy)**	**Reference**
IRAC	3.6	0.000374	[62]
IRAC	4.5	0.000241	[62]
IRAC	5.2	0.000374	[62]
IRAC	8	0.000241	[62]
2MASS	1.25	0.00295	[62]
2MASS	1.65	0.00171	[62]
2MASS	2.17	0.00101	[62]
WISE	3.4	0.000350	[62]
WISE	4.6	0.00252	[62]
WISE	12	0.002260	[62]
WISE	22	0.095900	[62]

3.7.2 Far infrared Data

Table 3.3: Far Infrared Data Measuring From Different Missions

Missions	**Wavelength (μm)**	**Flux (Jy)**	**Reference**
IRAC	60	162.3	[25]
IRAC	100	312.8	[25]
PASS	70	143.6	[25]
Pass	160	302.0	[25]
SPIRE	250	126.7	[25]
SPIRE	350	69.4	[25]
SPIRE	500	30.6	[25]
PLANCK	350	72.0	[25]
PLANCK	550	24.50	[25]
PLANCK	849	8.83	[25]
PLANCK	1382	3.27	[25]
PLANCK	2096	1.15	[25]
PLANCK	2998	0.93	[25]

3.8 Data Reduction and Obtaining Process

To extract and calculate data from the FITS file, we used two software programs - Aladin v10.0 and Python 3.7. Aladin v10.0 is a popular data reduction application that analyzes data collected by telescopes across all wavelengths. It examines each pixel of the FITS image and provides information such as the energy spectrum and relative flux density with pixel coordinates. We used Aladin v10.0 to obtain the flux and coordinate from the FITS image. Then, we used Python 3.7 to find the flux ratio and calculate various parameters such as dust temperature and dust mass. We plotted the color map and Gaussian functions of flux, temperature, and dust mass using Matplotlib. For dust modeling, we used the 2-Dust code.

3.8.1 The 2-Dust Code

The 2-Dust program, which takes into account a completely three-dimensional radiation field, solves the radiative transfer equation and derives the radiation and temperature fields within a two-dimensional polar grid. The program is designed in Fortran 90 to enable dynamic memory allocation for parameter arrays and is based on the iterative technique described by Collison and Fix [63]. Due to its simplicity and ease of use, we chose the long characteristic approach over alternative two-dimensional radiative transfer methods such as the moment method (Spagna, Leung, and Egan 1991), the short characteristic method (Kunasz and Auer), and the Monte Carlo method (Lefèvre, Daniel, and Bergeat 1983) [64, 65, 66]. Since this method tends to be computationally expensive, it has not been frequently employed. However, this issue can be resolved by parallelizing the code and utilizing the algorithm's heavily looped design.

By identifying the inner radius of the circumstellar shell as an observable that can be measured from high-resolution mid-IR images, we take a novel approach to this problem. The dust temperature at the inner radius can be specified nearly instantly once the inner shell radius has been established by observation. After that, it is pretty simple to derive the temperature and radiation field inside the shell. Alternately, the inner shell radius can be set by, for instance, assuming that the dust temperature at the inner radius is equal to the dust condensation temperature. The dust shell is not necessarily physically disconnected from the central source in this scenario, as the inner border of the shell does not line up with the dust condensation radius. The inner shell radius may be determined by the dust condensation radius, as in the dust-forming circumstellar wind shells; by a precipitous density drop caused by the cessation of mass loss, as in the detached shells; or by the swept-up shell boundary caused by a sudden mass ejection. Our method is general and does not require any assumptions.

Then, using the spectral energy distribution (SED) and the mid-IR images as constraints, we iterate on the model parameters. The dust shell's energetics are severely constrained by the measured inner shell radius, which also makes it possible to thoroughly examine the dust mineralogy (composition and size distribution). The axisymmetric dust distribution of the model is further constrained by the mid-IR images, and doing so would help to separate the combined impacts of the optical depth and the shell's inclination angle from the projected shell morphologies [67].

To be able to execute the program (2-Dust code) for our Helix, it is necessary to create several input parameter files some are collected from the Mishra, A., Li, A., and Jiang, B. W. (2016) [68], and some are collected from the different literature are in Appendix A. After compiling this program we get the numbers of output files, among these, we use the output file '7293-spec.dat' called spectral energy distribution (SED) to the fit. More details about the 2-Dust code and input−output files are explained in the 2-Dust users' manual [69].

Chapter 4

Results and Discussion

The study focused on understanding the properties of dust in the Helix Nebula (NGC-7293). To achieve this, the researchers used data from three surveys: IRIS, AKARI, and WISE. We also used a computer program called 2-Dust, which is written in a programming language called Fortran. We also calculated the dust color temperature, dust mass, Planck function, Jeans mass, and Jeans length using Aladin v10.0 and Python 3.7, and then we plotted the counters map of flux density, dust temperature, and dust mass using matplotlib in a Jupyter notebook. Finally, we analyzed the Gaussian nature of the dust mass, dust temperature, and flux using the Gaussian function, $F(x) = \frac{1}{\sqrt{2\pi\sigma}} exp(\frac{x-\hat{x}}{2\sigma})^2$. Where $\hat{x}$ and σ are mean value and standard deviation respectively. We used the 2-Dust model to fit the calculated SED data, photometry data, far infrared, and ISO SED data using the equation (3.1) which gives the density distribution function.

4.1 Distribution of Flux F60, F90, and F12 Micron

We are curious about the relative flux density radiated from each pixel inside the contour's dust structure. The contour plots of flux density variation in IRIS F60 μm, AKARI F90 μm, and WISE F12 μm are shown in Fig. 4.1 (a), (b), and (c) respectively, along with the color axis, X-axis represents R.A. (J2000), the Y-axis Decl. (J2000), and the projection of the Z-axis represents the flux density distribution. These figures provide details on the flux distribution in several geographical areas. The flux density increases from violet to red. The value of relative flux density obtained from F60 μm, F90 μm, and F12 μm FITS images are visualized using the Aladin v10.0 and plotted in Python 3.7. The regions

having a high relative flux density and a low relative flux density are represented by different colors. The color map of relative flux density covers the entire region of interest is presented in Fig.4.1.

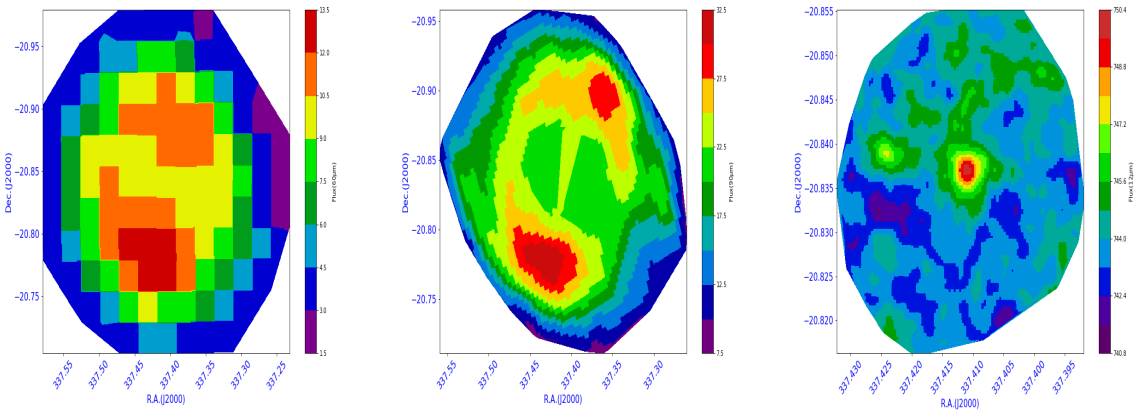

(a) **(b)** **(c)**

Figure 4.1: The contour plot of flux density variation (a) R.A.(J2000) versus Decl. (J2000) versus F60 μm in IRIS (b) R.A.(J2000) versus Decl. (J2000) versus F90 μm in AKARI and (c) R.A.(J2000) versus Decl. (J2000) versus F12 μm in WISE at R.A.(J2000). The color bar indicates the flux density as it increases from violet to red.

From Figure 4.1, it is seen that the relative flux density in the case of the IRIS and WISE survey is maximum around the central region and has a minimum around the outer region, but in AKARI, the maximum relative flux is not around the central region because of the dust particle having flux emission in this wavelength is not found around the central region. The maximum and minimum flux in IRIS at 60 μm is 13.25 MJy/sr and 1.96 MJy/sr. Similarly, in AKARI at 90 μm the maximum and minimum fluxes are 32.18 MJy/sr and 8.02 MJy/sr. In WISE, 749.90 MJy/sr and 241.51 MJy/sr are the minimum and maximum flux at 12 μm respectively with the correction of the mean value.

4.2 Distribution of Flux F100, F140 , and F22 Micron

Fig. 4.2 (a), (b), and (c) show the flux density distribution in the IRIS, AKARI and WISE maps, where R.A.(J2000) is plotted along X-axis and Decl. (J2000) along Y-axis and flux density distribution along Z-axis, the contour map gives the variation in flux density with different contour levels. From the Fig. 4.2, it is seen that the relative flux density

is maximum around the central region and a minimum around the outer region at F100 μm and F22 μm FITS image, but the relative flux density is minimum around the central region and maximum in the outer region at F140 μm. This indicates that the dust particles, which emit Flux at 100 μm and 22 μm are maximum in the central region of the helix nebula. Similarly, the dust particle which emits flux at 140 μm is minimum in the central region.

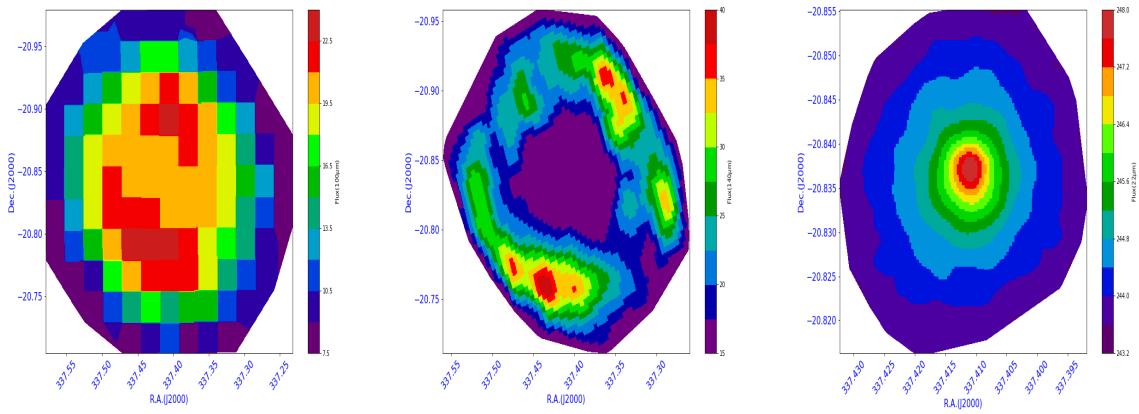

(a) **(b)** **(c)**

Figure 4.2: The contour plot of flux density variation (a) R.A.(J2000) versus Decl. (J2000) versus F100 μm in IRIS (b) R.A.(J2000) versus Decl. (J2000) versus F140 μm in AKARI and (c) R.A.(J2000) versus Decl. (J2000) versus F22 μm in WISE at R.A.(J2000). The color bar indicates the flux density as it increases from violet to red.

The maximum and minimum flux in IRIS at 100 μm is 23.58 MJy/sr and 7.60 MJy/sr respectively. Similarly, in the case of AKARI, 140 μm the maximum and minimum fluxes are 39.35 MJy/sr and 15.37 MJy/sr respectively. In WISE, the maximum and minimum fluxes are 247.97 MJy/sr and 243.60 MJy/sr at 22 μm. Also, in these wavelengths, the relative flux density of WISE is higher than that of AKARI, and AKARI has a higher relative flux density than IRIS.

4.3 Distribution of Dust Color Temperature

We estimated the dust color temperature of each pixel in the region of interest using equations (2.8), (2.10), and (2.12) for IRIS, AKARI, and WISE respectively. The plot of

the contour map using matplotlib in Python 3.7

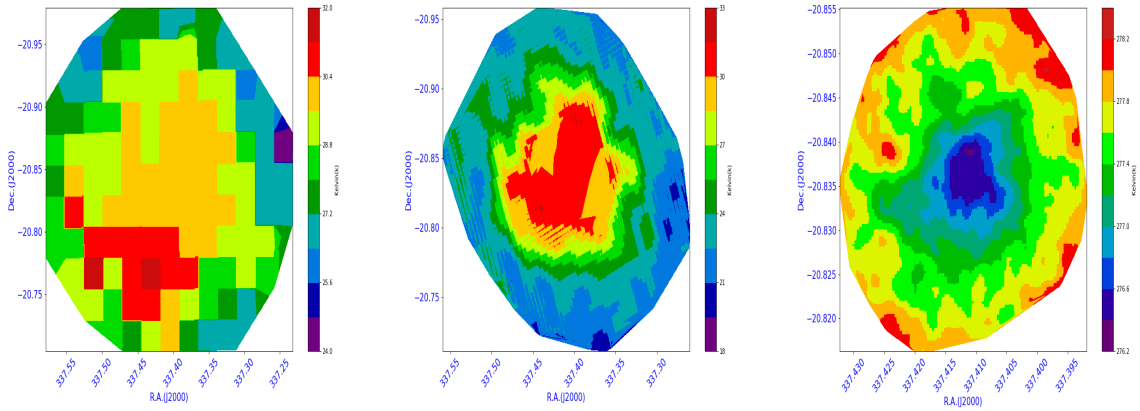

(a) **(b)** **(c)**

Figure 4.3: The contour plot of (a) R.A.(J2000) vs Decl. (J2000) vs Temperature in IRIS (b) R.A.(J2000) versus Decl. (J2000) versus Temperature in AKARI and (C) R.A.(J2000) versus Decl. (J2000) versus Temperature in WISE at R.A.(J2000)

Fig. 4.3 (a), (b), and (c) shows the variation of dust color temperature in IRIS, AKARI, and WISE surveys respectively. In these figures, R.A. is plotted along the X-axis, Decl. is along the Y-axis, and dust color temperature is plotted as the projection of the Z-axis along with a color bar scale. The distribution of temperatures shows that the core region is hot and the lower region is cold. In the case of Akari, maximal, minimal, and mean temperatures are (32.020 ± 0.078) K, (19.380 ± 0.078) K, and (24.440 ± 0.078) K respectively. Similarly, for the IRIS maximum, minimum, and mean temperatures are (31.690 ± 0.005) K, (24.530 ± 0.005) K, and (28.930 ± 0.005) K. The maximum, minimum, and mean temperatures for WISE are found to be (278.210 ± 0.001) K, (276.350 ± 0.001) K, and (277.490 ± 0.001) K, respectively. The minimum temperature zone indicates the presence of cold dust, whereas the highest temperature region reveals the presence of warm dust. As we have from equation (2.8), the temperature is inversely proportional to the wavelength, so the temperature in WISE is found to be higher than that of the IRIS and AKARI map. According to our findings, the dispersion of dust color temperature in the core of the Helix Nebula is characterized by a minimum value in WISE and a maximum value in IRIS and AKARI surveys. This is because the concentration of dust particles that emit at higher wavelengths is highest in the core and decreases towards the outer regions of the nebula. Conversely, the concentration of dust particles that emit at lower wavelengths is

also highest in the core and decreases towards the outer regions of the nebula. In higher wavelengths, the dust temperature agrees with Steene et al. (2015) [25]. They analyzed Herschel imaging of dust in the Helix Nebula (NGC 7293) utilizing the Pictures at 70, 160, 250, 350, and 500 μm were taken using the PACS and SPIRE instruments on board the Herschel satellite and discovered that the dust temperature ranges between 22 K to 42 K.

4.4 Distribution Map of Dust Mass

Steene et al. (2015) [25] calculated that the total dust mass of the Helix Nebula, excluding the halo, is 3.5$\times$ 10^{-3} solar masses at a distance of 216 pc. On the other hand, Meaburn et al. (1992) estimated that the total mass of one globule in the nebula is greater than or equal to 1.0$\times$ 10^{-5} solar masses, and the mean mass density is 6.2$\times$ 10^{5} cm^{-3} by assuming a standard interstellar dust mass ratio and reddening laws. In this work, we found that the total mass of the helix nebula using IRIS, AKARI, and WISE survey is 1.97×10^{29} kg, 1.12×10^{30} kg, and 6.85×10^{28} kg which is equivalent to 0.10 $M_{\odot}$, 0.56 $M_{\odot}$, and 0.034 $M_{\odot}$ respectively. The contour map of dust mass distribution is shown in Fig. 4.4
The contour plots of the distribution of dust mass in the IRIS, AKARI, and WISE maps can be seen in Fig. 4.4 (a), (b), and (c), where R.A. (J2000) is displayed along the x-axis, Decl. (J2000) is plotted along the y-axis, and dust mass is plotted along the z-axis. The contour plot helps in determining the values of mass. In AKARI, the maximal and minimal dust mass is 3.22×10^{25} kg and 2.07×10^{24} kg respectively. Similarly, in IRIS, the maximum and minimum dust mass is 4.04×10^{24} kg and 1.43×10^{24} kg, and in WISE, 6.22×10^{23} kg is the maximum and 6.07×10^{23} kg is the minimum value of dust mass in the Helix Nebula NGC 7293 respectively. The AKARI data indicates that the dust grains in the upper regions have a higher mass compared to the lower regions, and the central region has the least amount of dust mass. On the other hand, the IRIS and WISE surveys show that the greatest number of dust grains are located in the central region, while the outer regions have the least amount of dust grains.

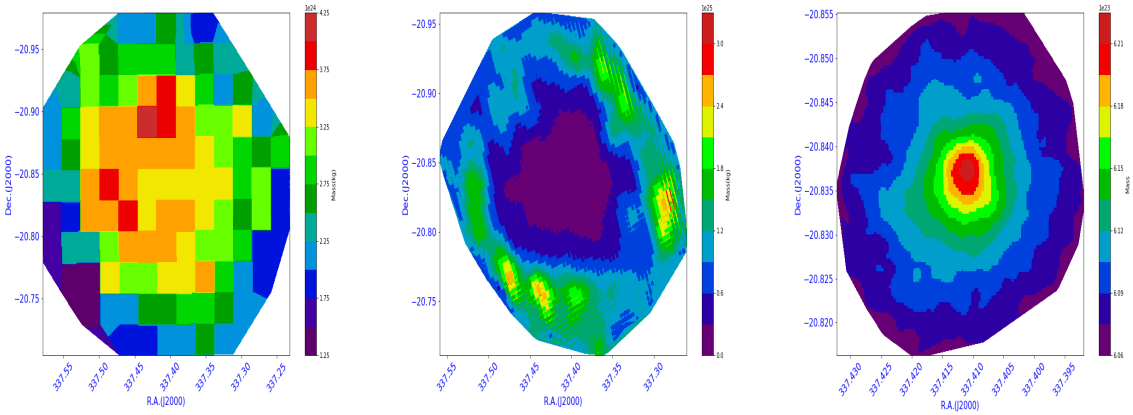

(a) **(b)** **(c)**

Figure 4.4: The contour plot of (a) R.A.(J2000) vs Decl. (J2000) vs Mass in IRIS (b) R.A.(J2000) versus Decl. (J2000) versus Mass in AKARI and (C) R.A.(J2000) versus Decl. (J2000) versus Mass in WISE at R.A.(J2000). The value of mass is average at the center in IRIS and is minimum at the center in AKARI)

4.5 Gaussian Nature of Dust Color Temperature

The variation of dust color temperature of data follows the Gaussian nature as shown in the figures below. In the figures, the horizontal axes represent the values of the variables being described (Temperature). The vertical axes represent the probability of occurrence of each of the values of the variable.

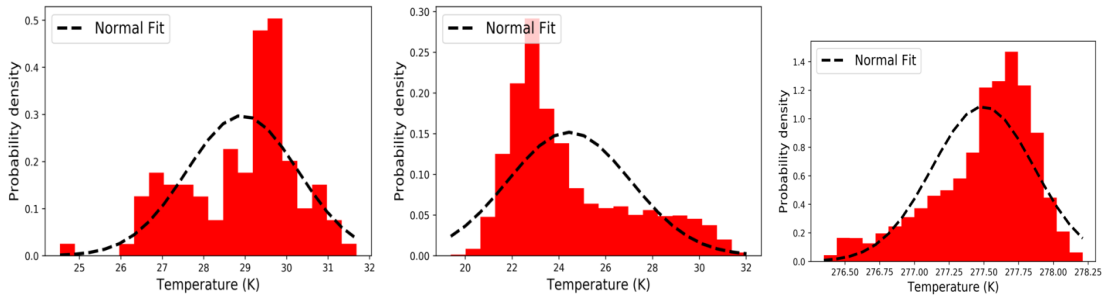

(a) **(b)** **(c)**

Figure 4.5: Gaussian with histogram displays of (a) Temperature vs probability density function in IRIS, (b) Temperature versus probability density function in AKARI, and (c) Temperature versus probability density function: WISE.

Figure 4.5 (a), (b), and (c) present a Gaussian plot that shows the relationship between

temperature and probability density function, along with a corresponding histogram. The curve is slightly skewed to the left in IRIS and slightly skewed to the right in AKARI surveys, while in the WISE survey, it is left-skewed. The center of the Gaussian distribution is found to be (28.930 ± 0.005) K in IRIS, (24.440 ± 0.078) K in AKARI, and (277.490 ± 0.001) K in WISE.

4.6 Gaussian Nature of Dust Mass

The variation of dust mass of data follows the Gaussian nature as shown in the figures below. In the figures, the horizontal axes represent the values of the variables being described (Mass). The vertical axes represent the probability of occurrence of each of the values of the variable. The curve is slightly skewed to the left in IRIS, right in AKARI, and also right skewed in WISE.

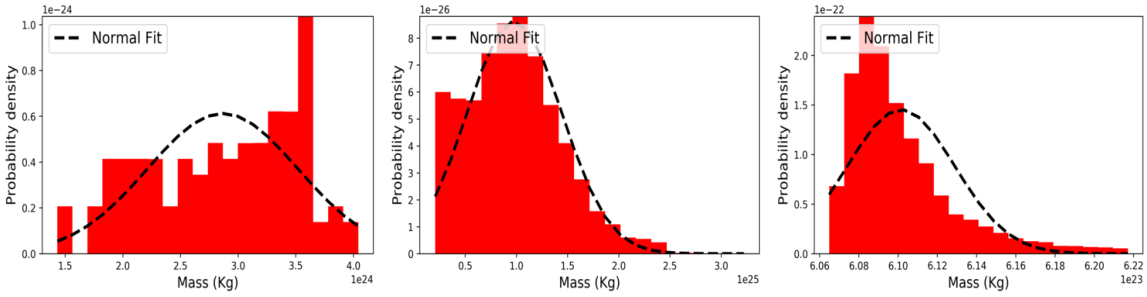

(a) **(b)** **(c)**

Figure 4.6: Gaussian with histogram, plot (a) Mass vs s probability density functions in IRIS (b) Mass vs probability density function in AKARI and, Plot (c) Mass vs probability density function in WISE.

The Gaussian with histogram plot of Mass is displayed in Fig. 4.6 (a), (b), and (c) plotted with the help of a Jupyter Notebook. The Gaussian center is found to be 2.87×10^{24} kg in IRIS, 9.80×10^{24} kg in AKARI, and 6.10×10^{23} kg in the WISE survey.

4.7 Gaussian Nature of F60, F90, and F12 Micron

Fig. 4.7 (a), (b), and (c) is the Gaussian plot of 60 μm, 90 μm, and 12 μm with histogram respectively. The Gaussian center is found to be 7.44 MJy/sr in IRIS, 20.25 MJy/sr in the

AKARI and 743.96 MJy/sr in the WISE survey. The probability density function versus flux graph is more or less normally distributed in IRIS, AKARI, and WISE.

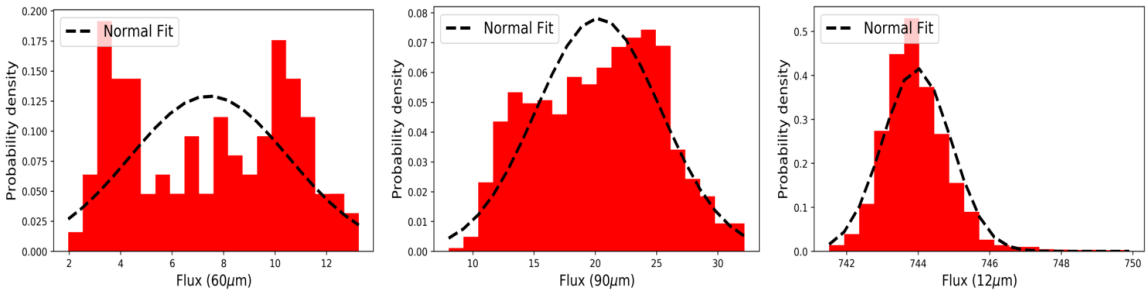

(a) **(b)** **(c)**

Figure 4.7: Gaussian plot with a histogram for the flux measurements of different wavelengths in the IRIS, AKARI, and WISE surveys. Specifically, it shows the probability density functions for F60 μm in IRIS, F90 μm in AKARI, and F12 μm in WISE.

4.8 Gaussian Nature of F100, F140, and F22 Micron

Fig. 4.8 (a), (b), and (c) is the Gaussian plot of 100 μm, 140 μm, and 22 μm with histogram respectively. The Gaussian center is found to be 115.36 MJy/sr in IRIS, 22.73 MJy/sr in the AKARI and 244.37 MJy/sr in WISE survey. The probability density function versus flux graph is normally distributed in IRIS and slightly skewed to the right in AKARI and WISE.

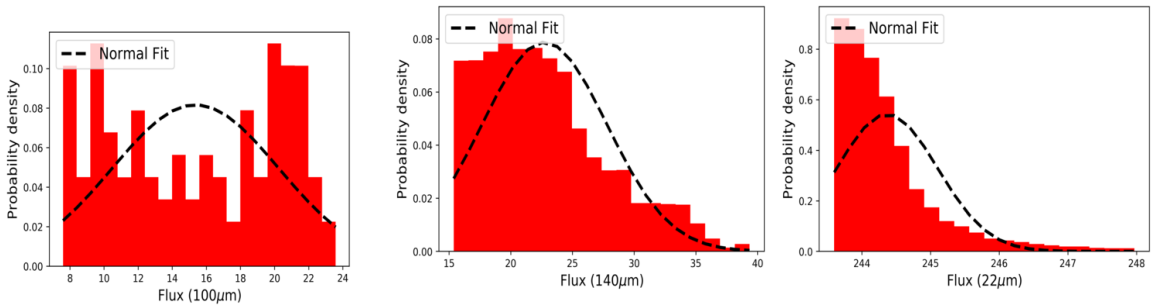

(a) **(b)** **(c)**

Figure 4.8: Gaussian plot with a histogram for the flux measurements of different wavelengths in the IRIS, AKARI, and WISE surveys. Specifically, it shows the probability density functions for F100 μm in IRIS, F140 μm in AKARI, and F22 μm in WISE.

4.9 Jeans Mass and Jeans length

The Jeans Mass of this nebula is calculated using the equation,

$$M_J = \left\{ 6\frac{\mathrm{k}T}{\mu \mathrm{m_H G}} \right\}^{\frac{3}{2}} \left\{ \frac{3}{4\pi\rho} \right\}^{\frac{1}{2}} \tag{4.1}$$

Here, Boltzmann constant (k) = $1.38\times10^{-23} JK^{-1}$ the mean temperature of our source in Akari survey (T) = 24.44 K, mean molecular weight of hydrogen gas ($\mathrm{m_H}$) = 1.67×10^{-27} kg, and Gravitational constant (G) = 6.67×10^{-11} $\mathrm{Nm}^2 kg^{-2}$. We determine the density of the nebular cloud by using the equation,

$$\rho = \left\{ \frac{3}{4\pi} \right\}^{\frac{2}{3}} \frac{\mathrm{k}T}{\mathrm{m_H G}R^2} \tag{4.2}$$

Specifically, the average radius of our source R = 5×10^{13} m [72]. Using equation (3.7), we get the density of our source is 4.66×10^{-13} kg m^{-3} This density statistic represents the average density of dust in ISM. Using the density value in equation (3.8) we found the Jeans' mass ($\mathrm{M_J}$) is 4.65 M⊙. Similarly, we calculate Jena's length by using the equation,

$$\lambda_j = \left[\frac{9\mathrm{k}T}{2\pi\mu \mathrm{m_H G}\rho} \right]^{\frac{1}{2}} \tag{4.3}$$

and we get the value of Jean's length is 2.71×10^{14} m.

Since the predicted mass of our nebula is 0.56 $\mathrm{M}_\odot$ using the AKARI survey, which is less than Jean's mass, as well as the radius is 2.71×10^{14} m, which is more than Jean's length. We infer that the helix nebula may not be a star-forming zone based on our computation of Jean's mass and Jeans's length.

4.10 2-Dust Modelling of Helix

Our first axisymmetric model for the Helix Nebula (NGC 7293) is presented here, along with thorough comparisons to other models. It is believed that the Helix Nebula has a shape similar to a flattened sphere, with areas of high density concentrated towards the center of the disk along its equatorial plane. The Helix Nebula is considered the most advanced planetary nebula among the observed ones. It has a large spatial extent, with low electron density, and is almost entirely ionized, indicating a high degree of ionization. Additionally, it is enveloped in a layer of predominantly cool dust [70]. Previous model

computations for the Helix Nebula (NGC 7293) have assumed spherical symmetry, simple blackbody approximations, and the dust disk model. In this model, we have used calculated SED data, photometric data, far infrared, and ISO spectra (SED) data of Helix which are in good agreement, as illustrated in Fig. 4.10. In this figure ISO SED data of Helix(7293) used in the plot are shown in Appendix B Table 1. The model calculated SED is shown in sky-blue soiled lines and the data is in Appendix B Table 2. The ISO IR spectrum solid grey line is from the wave site [73]. The photometry data (2Mass in the green square, wise in the blue star, and Irac in the red triangle) values are shown in Table 3.3. The far Infrared data (Pacs in pinky diamond, Irac in navy Hexagon, Spire in black circle, and Planck in orange triangle) values are shown in Table 3.4. This model shows only the gross dust features such as the broad amorphous silicate bands at 0.005 μm and 0.1 μm, which was given in Table 3.1. Our result differs from other works which may be due to the consideration of the axis symmetry model which results in different grain parameters. When rescaled appropriately for differences in assumed temperature, a_{max}, our derived physical parameters are comparable to Speck et al. (2002) [29] and Planck collaborations Arnaud et al.(2015) [70] are shown in Table 4.1. Speak et al. conducted a study on the Helix Nebula (NGC 7293), where they analyzed the large-scale extended emission around it. The study focused on observing the ionized gas, molecular gas, and cool dust in the nebula. To analyze the emission in H_α, they used radiative transfer modeling, assuming that the outer layers of the circumstellar shell had a spherical symmetry. They created a H_α image using images from the Southern H_α Sky Survey Atlas. The molecular emission was mapped using the H_2 v=1$\rightarrow$0 S(1) line at 2.122 μm. The far-infrared observations were obtained using ISOPHOT on the Infrared Space Observatory. On the other hand, Arnaud et al. [70] researched the millimeter and sub-millimeter emissions from planetary nebulae in their study of Planck intermediate results. They were able to determine the density, spatial distribution, and total mass of ionized gas in these nebulae. They also calculated the internal radius, the extent of the dusty envelope, and its mass content using free-free emission and the DUSTY code.

Using the axisymmetric model mass loss rate of the Helix is found to be 1.04×10^{-5} $M_\odot$ yr^{-1}, and the radius, inner shell size, and outer shell size of Helix are 1.67×10^9 cm, 1.20×10^{17} cm, and 9.58×10^{17} cm respectively. In 1980, Thompson and Sihna established a maximum value for the current mass loss rate of the central star in the Helix. They

determined that the upper limit was 2×10^{-6} $M_\odot$ yr^{-1} by examining the minimum levels of its radio emissions [71]. Similarly, in 2003, Steffen and López conducted research on the percolating winds passing through a clumpy torus. Using axisymmetric numerical hydrodynamical simulations, they found that the mass loss rate was 2.15×10^{-5} $M_\odot$ yr^{-1}. This was calculated based on a power law density fall off of the index -1.9 [72]. In 1992, Meaburn and colleagues studied the presence of dust in the neutral globules of the Helix Nebula, NGC 729. Through their research, they determined that the mass loss rate was 10^{-5} $M_\odot$ yr^{-1}.

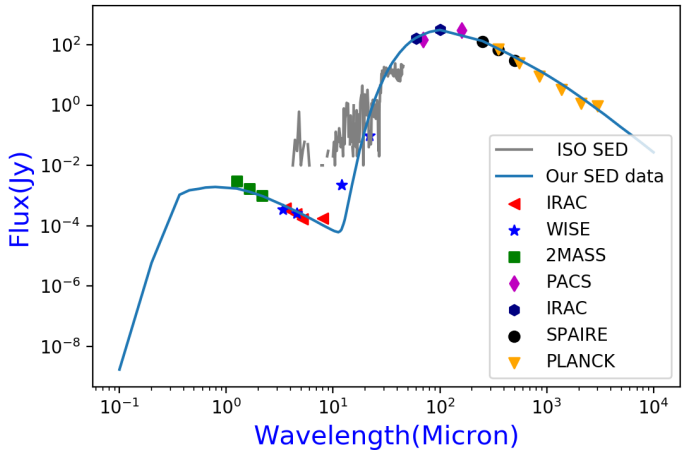

Figure 4.9: Comparison of the model SEDs with the broadband photometry of IRAC, WISE, 2Mass, and far infrared broadband of PACS, IRAC, SPAIRE, and PLANCK as well as the ISO SEDs of Helix Nebula

Table 4.1: Comparison of our model and other models

Parameters	**Our Model**	**Simple radiative transfer model (Speck et al.(2002))**	**DUSTY model (Arnaud et al.(2015))**
Distance	200 pc	200 pc	213 pc
Temperature(T_*)	120,000 K	123,000 K	110,000 K
Luminosity (L_*)	9.67 $L_\odot$	100 $L_\odot$	120 $L_\odot$
Grain size Distribution,n_g	$a^{-3.5}$	$a^{-3.5}$	$a^{-3.5}$
$a_{max}\mu m$	0.1	3.5	0.025
$a_{min}\mu m$	0.005	0.005	0.005
Peak Density	3.5 gm cm^{-3}	60 gm cm^{-3}	3 gm $cm^{-3}$for silicate and $2gmcm^{-3}$for carbon
Mass in Circumstellar shell	0.051 $M_\odot$	1.3 $M_\odot$	$18\times10^{-4}M_\odot$
Optical depth	0.12	-	0.0085
R_{in}	40		140 arcsec

Chapter 5

Conclusions and Recommendations

5.1 Conclusions

The goal of this study is to look into the physical properties of the planetary nebula as well as simulate the dust with the 2-Dust code. For our far-infrared analysis, we picked the Helix Nebula (NGC 7293) at 60 μm and 100 μm in the IRIS survey, 140 μm and 90 μm in the AKARI survey, and 22 μm and 12 μm in the WISE survey. Similarly, we fit photometry, far infrared, and ISO spectra, and compute SED data. This dissertation calculates the dust color temperature, dust mass, brightness of the central star of Helix, and mass loss rate. The variation in dust temperature, mass, Planck's function, and flux density was calculated, and the findings were compared and evaluated using IRIS, AKARI, and WISE.

- The study found that the dust color temperature of the Helix Nebula varies depending on the survey used. In the IRIS survey, the range was between (31.690 ± 0.005) K − (24.530 ± 0.005) K, with an average dust color temperature of (28.930 ± 0.005) K. In the AKARI survey, the range was between (32.020 ± 0.078) K − (19.380 ± 0.078) K, with an average dust color temperature of (24.440 ± 0.078) K. In the WISE survey, the range was between (278.210 ± 0.001) K − (276.350 ± 0.001) K, with an average dust color temperature of (277.490 ± 0.001) K. For higher wavelengths, our calculated temperature agrees with the work of Steene et al. (2015) [25] which was found to be 22 K to 42 K

- The study found that the dust color temperature was higher in the WISE survey than

in the IRIS and AKARI surveys. This suggests an inverse relationship between the dust color temperature and the wavelength.

- Based on the IRIS survey, the study found that the dust mass of Helix was 1.97×10^{29} kg (0.10 $M_\odot$). The dust mass in the AKARI survey was determined to be 1.12×10^{30} kg (equivalent to 0.56 $M_\odot$), whereas, in the WISE survey, it was found to be 6.85×10^{28} kg (equivalent to 0.034 $M_\odot$). This suggests that the dust mass value is higher in the AKARI survey and lower in the WISE survey. The Helix Nebula has been estimated to have a mass of 0.051 $M_\odot$ using an axisymmetry model. This is comparable to Speck et al. (2002) [29], who conducted research on the Helix Nebula (NGC 7293) and analyzed the extended emission around it using a simple radiative transfer model. They estimated that the dust mass of the nebula was 1.4 $M_\odot$, and Arnaud et al. (2015) [70], used the Dusty code to study the millimeter and sub-millimeter emissions from planetary nebulae, and their research showed that the dust mass of the Helix Nebula was 0.0018 $M_\odot$.

- Our computation of Jean's mass and Jean's length leads us to infer that the Helix Nebula is unlikely to be a region where stars are formed.

- Based on the axisymmetric model, the estimated mass loss rate of the Helix Nebula is 1.04×10^{-5} $M_\odot$ yr^{-1}. The radius, inner shell size, and outer shell size of the Helix are 1.67×10^{9} cm, 1.20×10^{17} cm, and 9.58×10^{17} cm, respectively. Similarly, luminosity is 9.67 $L_\odot$, and maximum and minimum dust grain sizes were found to be 0.1 μm and 0.005 μm.

5.2 Recommendations

This research has provided valuable insights and knowledge, which can be used to enhance future research on the topic. One such direction could be to carry out:

- Similar work using different surveys such as the Spitzer Telescope and 2MASS. This can help to validate the findings of this research and provide a more comprehensive understanding of the Helix Nebula.
- In addition to conducting similar work using different surveys, future research could also involve simulating the Helix Nebula using the Dusty code and comparing it to the 2-Dust code. This can help us better understand the physical processes and mechanisms that govern nebula creation and development and also provide insights into the accuracy and reliability of different modeling techniques. The comparison of the two models can reveal the strengths and limitations of each approach and help researchers to identify areas where improvements can be made. Ultimately, this can lead to a more comprehensive and accurate understanding of the Helix Nebula and other planetary nebulae.

References

[1] E. Dwek, *Interstellar dust: what is it, how does it evolve, and what are its observational consequences?*, AIP, **761**, 103-122 (2005).

[2] R. J. Trumpler, *Preliminary results on the distances, dimensions and space distribution of open star clusters*, HUP, **14**, 154-188 (1930).

[3] H. Karttunen, P. Kröger, H. Oja, M. Poutanen, & K. J. Donner, *Fundamental astronomy*, Springer (2007).

[4] https://ned.ipac.caltech.edu/level5/Fitzpatrick/Figures/figure1.gif (Viewed on July, 2022).

[5] J. A. Cardelli,G.C. Clayton, & J. S. Mathis, *The relationship between infrared, optical, and ultraviolet extinction*, APJ, **345**, 245-256 (1989).

[6] D. P. Cox, *The Three-Phase Interstellar Medium Revisited. Annual Review of Astron and Astrophys*, **43**, 337-385 (2005).

[7] A. G. Tielens, *The physics and chemistry of the interstellar medium*, CUP (2005).

[8] S. R. Coe, *What Are All These Different Types of Nebulae, and What Details Can I See in Them with My Telescope?*, Springe 133-177 (2016).

[9] D. E. Osterbrock, *Book Review: Astrophysics of Gaseous Nebulae and Active Galactic Nuclei./University Science Books, 1988.* JRASC, **83**, 345-347 (1989).

[10] S. Kwok, *Planetary nebulae: A modern view*, PSAP, **106**, 344 (1994).

[11] A. Frank, B. Balick, V. Icke, & G. Mellema, *Astrophysical gas dynamics confronts reality-The shaping of planetary nebulae*, AJ, **404**, L25-L27 (1993).

[12] S. Kwok, *The Origin and Evolution of Planetary Nebulae*, CUP (2001).

[13] J. L. Hora Latter, W. B. Smith, H. A. & M. Marengo,*Infrared observations of the helix planetary nebula*, ApJ, **652**, 426 (2006).

[14] L. N. Zack, *Laboratory and Observational Studies of Transient Molecules at Microwave and Millimeter/Submillimeter Wavelengths*, Doctoral dissertation, The University of Arizona), United States (2012).

[15] R. B. C. Henry, K. B. Kwitter, & R. J. Dufour, (1999). *Morphology and composition of the helix nebula*, ApJ, **517**, 782(1999).

[16] C. R. O'Dell, P. R. McCullough, & M. Meixner, *Unraveling the Helix Nebula: its structure and knots*, AJ, **128**, 2339 (2004).

[17] C. R. O' Dell, W.J. Henney, & G. J. Ferland, *A multi-instrument study of the helix nebula knots with the Hubble space telescope*, AJ, **130**, 172 (2005).

[18] P. J.Huggins, R. P.Bachiller, P. Cox & T. Forveille, *CO in the cometary globules of the Helix Nebula*, AJ, **401**, L43-L46 (1992).

[19] M. Matsuura, A. K. Speck, B. M. McHunu, I. Tanaka, N. J.Wright, M. D. Smith, & R. Wesson, *A "Firework" of H_2 Knots in the Planetary Nebula NGC 7293 (The Helix Nebula)*, ApJ, **700**, 1067 (2009).

[20] E. R. Capriotti & A. D. Kendall, *The origin and physical properties of the cometary knots in NGC 7293*, AJ, **642**, 923 (2006).

[21] M. Matsuura, A. K. Speck, M. D. Smith, A. A. Zijlstra,S. Viti, K. T .E. Lowe & E. Lagadec, *VLT/Infrared Integral Field Spectrometer Observations of Molecular Hydrogen Lines in the Knots in the Planetary Nebula NGC 7293 (the Helix Nebula)*, (2007).

[22] https://i.gadgets360cdn.com/large/nasa nebula photo instagram 1635847930915.jpg (viewed on 13 July, 2022).

[23] J. Meaburn, C. A. Clayton, C. M. Bryce, & J. R. Walsh, *The global motions of the cometary knots in the Helix planetary nebula (NGC 7293)*, Mon. Not. R. Astron. Soc., **281**, L57-L61 (1996).

[24] J. R. Meaburn, R. E. S. Walsh, N. A. Clegg, D. Walton, Taylor & D. S. Berry, *Dust in the neutral globules of the Helix nebula, NGC 7293*, Mon. Not. R. Astron. Soc., **255**, 177-182 (1992).

[25] G. C. Van de Steene, P. A. M. Van Hoof,K. M. Exter, M. J. Barlow, J. Cernicharo, M. Etxaluze & P. C. Hargrave, *Herschel imaging of the dust in the Helix nebula (NGC 7293)*, A & A, **574**, A134 (2015).

[26] J. H. Cahn, & J. B. Kaler, *The distances and distribution of planetary nebulae*, Astrophys. J. Suppl. Ser **22**, 319 (1971).

[27] C.T. Daub, *A statistical survey of local planetary nebulae*, APJ, **260**, 612-624 (1982).

[28] C.Y. Zhang, & S. Kwok, *Trace of planetary nebula evolution by distance-independent parameters*, ApJS, **88**, 137 (1993).

[29] A. K. Speck, M. Meixner, D. Fong, P. R. McCullough, D. E. Moser, & T. Ueta, *Large-scale extended emission around the Helix Nebula: dust, molecules, atoms, and ions*, AJ, **123**, 346 (2002).

[30] C. A. Beichman, R. W. Wilson, W. D. Langer, & P. F. Goldsmith, *Infrared limb brightening in the Barnard 5 cloud*, APJ, **332**, L81-L85 (1988).

[31] J. L. Puget, A. Leger, & F. Boulanger, *Contribution of large poly- cyclic aromatic molecules to the infrared emission of the interstellar medium*, A & A, **142**, L19-L22 (1985).

[32] W. D. Langer, R. W. Wilson, P. F. Goldsmith, & C. A. Beichman, *Dust and gas emission in Barnard 5*, AJ, **337**, 355-381 (1989).

[33] D. O. S. Wood, P. C. Myers, & D. A. Daugherty, *IRAS images of nearby dark clouds*, APJS , **95** , 457-501 (1994).

[34] B.T. Draine, & H. M. Lee, *Optical properties of interstellar graphite and silicate grains*, APJ, **285**, 89-108 (1984).

[35] X. Dupac, J. P. Bernard, N. Boudet, M. Giard, J. M. Lamarre, C. Mény, & J. P. Torre, *Inverse temperature dependence of the dust submillimeter spectral index*, A & A, **404**, L11-L15 (2003).

[36] R. H. Hildebrand, S. E. Whitcomb, R. Winston, R. F. Stiening, D. A. Harper, & S . H. Moseley, *Submillimeter photometry of extragalactic objects*, APJ, **216**, 698-705 (1077).

[37] K. Young, T. G. Phillips, & G. R. Knapp, *Circumstellar shells resolved in the IRAS survey data. I - Data processing procedure, results, and confidence tests*, APJS, **86**, 517-540 (1993).

[38] C. A. Beichman, R. W. Wilson, W. D. Langer, & P. F. Goldsmith, *Infrared limb brightening in the Barnard 5 cloud*, APJ, &332, L81-L85 (1988).

[39] M. A. Miville-Deschênes, & G. Lagache, *IRIS: a new generation of IRAS maps*, APJS **157**, 302 (2005).

[40] G. Neugebauer, H. Habing, R. Van Duinen, H. Aumann, B. Baud, C. Beichman, . . . others, *The infrared astronomical satellite (iras) mission*, APJ, **278**, L1–L6 (1984).

[41] https://d2pn8kiwq2w21t.cloudfront.net/originalimages/missionswebirasspFCsJR.jpg (viewed on November 29, 2022)

[42] https://encrypted-tbn0.gstatic.com/images q=tbn (viewed on November 29, 2022)

[43] A. Pouw, *The IRAS spacecraft. Journal of the British Interplanetary Society*, **36**, 17-20 (1983).

[44] https://irsa.ipac.caltech.edu/IRASdocs/exp.sup/ch2/figs/figC6-1.gif (viewed on November 29, 2022)

[45] K. J. Wildeman, D. A. Beintema, & P .R. Wesselius, *The Dutch Scientific Instrument on board IRAS*, JBIS, **36**, 21-26 (1983).

[46] H. Murakami, M.M. Freund, K. Ganga, H. Guo, T. Hirao, N. Hiromoto, . . . L. Yuen, *The IRTS (Infrared Telescope in Space) Mission*, PASG, **48**, L41-L46 (1996).

[47] M. Kawada, H. Baba, P. D. Barthel, D. Clements, M. Cohen, Y. Doi, . . . A. Yasuda, *The Far-Infrared Surveyor (FIS) for AKARI*, PASG, **59**, S389 (2007).

[48] T. Onaka, H. Matsuhara, T. Wada, N. Fujishiro, H. Fujiwara, M. Ishigaki, . . . Y. Ikeda, *The Infrared Camera (IRC) for AKARI – Design and Imaging Performance*, PASG, **59**, S401 (2007).

[49] T. Nakagawa, K. Enya, M. Hirabayashi, H. Kaneda, T. Kii, Y. Kimura, . . . S. Yoshida, *Flight Performance of the AKARI Cryogenic System*, PASH, **59**, S377-S387 (2007).

[50] T. Totani, T. T. Takeuchi, M. Nagashima, M. A. Kobayashi, & R. Makiya, *Infrared Spectral Energy Distribution of Galaxies in the AKARI All-Sky Survey: Correlations with Galaxy Properties, and Their Physical Origin*, PASG, **63**, 1181-1206 (2011).

[51] B. J. Smith, S. D. Price , & R. I. Baker, ApJS, **154**, 67 (2004).

[52] E. L. Wright, P. R. Eisenhardt, A. K. Mainzer, M. E. Ressler, R. M. Cutri, T. Jarrett, ... & C. W. Tsai, *The Wide-field Infrared Survey Explorer (WISE): mission description and initial on-orbit performance*, APJ, **140**, 1868 (2010).

[53] https://www.researchgate.net/profile/John−Mather2/publication/231092973/−figure/fig2/AS:669099399061521@1536537136540/Diagram−showing−the−WISE−flight−system−insurvey−configuration-with−cover−off−The.jpg (Viewed on November 25, 2022)

[54] E. L. Wright, *WISE: the Wide-field Infrared Survey Explorer. In Infrared Systems and Photoelectronic Technology IV*, SPIE, **7419**, 13-19, (2009).

[55] M. Meixner, T. Ueta, M. Bobrowsky, & A. Speck, *Two subclasses of proto-planetary nebulae: model calculations*, APJ, **571**, 936 (2002).

[56] K. Y. Su, Y. H. Chu, G. H. Rieke, P. J. Huggins, R. Gruendl, R. Napiwotzki, ...& K. Volk, *A debris disk around the central star of the helix nebula?*, APJ, **657(1)**, L41 (2007).

[57] M. Andriantsaralaza, A Zijlstra, & A. Avison, *CO in the C1 globule of the Helix nebula with ALMA*, Mon. Notices Royal Astron. Soc., **491**, 758-772 (2020).

[58] S. Kim, P. G. Martin, & P.D. Hendry, ApJ, **422**, 164 (1994).

[59] C. Dominik, E. Sedlmayr, & H. P. Gail, A &A, **223**, 227 (1989).

[60] T. Ueta, , et al. , ApJ, **557**, 831 (2001a).

[61] A. Agnès, & O. François, *Strasbourg-ESO catalogue of galactic planetary nebulae. In Planetary Nebulae (pp. 33-33)*, Springer, Dordrecht (1993).

[62] https://ned.ipac.caltech.edu (Viewed on February 9, 2023)

[63] A. J. Collison, & J. D. Fix, *Axisymmetric models of circumstellar dust shells*, APJ, **368**, 545-557 (1991).

[64] Jr. G. F. Spagna, C. M. Leung, & M. P. Egan, *Radiation transport in dust in disk geometry. I-Application to externally heated interstellar clouds*, APJ, **379**, 232-244 (1991).

[65] P. Kunasz, & L. H. Auer, *Short characteristic integration of radiative transfer problems: formal solution in two-dimensional slabs*, J Quant Spectrosc Radiat Transf, **39(1)**, 67-79 (1983).

[66] J. Lefevre, J. Y. Daniel, & J. Bergeat, *Numerical simulation of radiative transfer in circumstellar dust shells. II-Ellipsoidal shells*, A & A, **121**, 51-58 (1983).

[67] T. Ueta, & M. Meixner, *2-DUST: a dust radiative transfer code for an axisymmetric system*, APJ, **586**, 1338 (2003).

[68] A. Mishra, A. Li, & B. W. Jiang, *On the relation between the mysterious 21 μm emission feature of post-asymptotic giant branch stars and their mass-loss rates*, APJ, **825**, 68 (2016).

[69] https://www.researchgate.net/publication/2423516282DUSTADustRadiative TransferCodeforanAxisymmetricSystem (Viewed on March 23, (2023)

[70] M. Arnaud, F. Atrio-Barandela, J. Aumont, C. Baccigalupi, A. J. Banday, R. B. Barreiro, R. B., ... and M. Tucci, *Planck intermediate results. XVIII. The millimeter and sub-millimeter emission from planetary nebulae*, A & A, **573**, A6 (2015).

[71] A. R. Thompson, & R. P. Sinha, *An upper limit to the mass loss rate from the nuclei of planetary nebulae*, Astron. J., **85**, 1240 (1980).

[72] W. Steffen, & J. A. López, *Percolating Winds through a Clumpy Torus. Revista Mexicana de Astronomía y Astrofísica*, **15**, 50-52 (2003).

[73] https://irsa.ipac.caltech.edu/data/SWS/ (Viewed on January 12, 2023).

Appendix A

Input parameter files required for 2-Dust code.

Table A.1: Dates files.dat

0
7296
Cross-section File specgrid
quad48
7293_stuff
dprop
xsec
sourceflux

Table A.2: 7293.dat.file

48	8					
1000	0.0001					
0	0	0				
0.024	120000.0					
9	2	1.0	3	3	3	3
0.12	18					
40	5.5	1.0				
1						
4.0						

Table A.3: Drop.dat.file

1						
1						
1	3	1.0	3.5	0.005	0.1	nk_$aigen_data_modified$

Table A.4: Wavelength Grid File

0.1	3.75	11.2	20.8	36	500	4100
0.2	4.8	11.7	21	42	900	4900
0.365	5.2	12	21.5	48	1100	55000
0.45	5.8	12.5	23	55	1400	6200
0.556	6.3	12.89	24.5	60	1600	7000
0.64	7	15	25	65	19000	7810
0.79	8	17.4	27	80	2200	8700
1.25	8.5	17.72	30	100	2800	9200
1.65	9.8	18	31.5	250	3500	10000
2.2	10.3	19.5	33	450	4100	

Table A.5: Quadrature File, 'quad45.dat

SN.					SN.					SN.				
1	7	2	2	0.97	17	5	6	2	0.50	33	5	6	4	-0.87
2	7	2	2	0.91	18	5	6	2	0.49	34	5	6	4	-0.89
3	7	2	2	0.81	19	5	6	2	0.49	35	5	6	4	-0.91
4	7	2	2	0.71	20	5	6	2	0.51	36	5	6	4	-0.90
5	7	2	2	0.70	21	5	8	2	0.53	37	5	6	4	-0.92
6	7	2	2	0.70	22	5	8	2	0.42	38	5	6	4	-0.92
7	8	2	2	0.56	23	5	7	3	0.14	39	5	6	4	-0.91
8	7	2	2	0.46	24	5	6	4	-0.90 E-2	40	5	6	4	-0.92
9	7	2	2	0.48	25	5	6	4	-0.16	41	5	6	4	-0.92
10	7	2	2	0.52	26	5	6	4	-0.27	42	5	6	4	-0.93
11	7	3	2	0.51	27	5	6	4	-0.50	43	4	6	5	-0.94
12	7	4	2	0.49 7	28	5	6	4	-0.66	44	3	6	6	-0.96
13	6	4	2	0.50	29	5	6	4	-0.70	45	3	6	7	-0.97
14	5	4	2	0.50	30	5	6	4	-0.71	46	3	6	7	-0.98
15	5	4	2	0.50	31	5	6	4	-0.77	47	3	6	7	-0.98
16	5	4	2	0.50	32	5	6	4	-0.83	48	3	6	7	-0.98

Table A.6: Cross-section File

7.161203E-18

0.10000	2.246192E-12	6.906206E-13	4.069778E-02
0.20000	7.748864E-13	2.802089E-13	1.445789E-02
0.36500	2.271541E-13	1.396232E-13	4.613296E-03
0.45000	1.784761E-13	1.029951E-13	3.038599E-03
0.55600	1.395018E-13	7.539291E-14	2.010697E-03
0.64000	1.146742E-13	6.037769E-14	1.528311E-03
0.79000	8.941113E-14	4.000875E-14	1.011236E-03
1.25000	5.081879E-14	1.188565E-14	4.172473E-04
1.65000	3.497344E-14	4.408723E-15	2.447352E-04
2.20000	2.356682E-14	1.435201E-15	1.409750E-04
3.45000	1.400918E-14	2.385263E-16	5.912836E-05
3.75000	1.250778E-14	1.720224E-16	5.047164E-05
4.80000	9.032138E-15	6.478986E-17	3.137318E-05
5.20000	8.153554E-15	4.711325E-17	2.684175E-05
5.80000	7.151559E-15	3.045201E-17	2.165815E-05
6.30000	6.656417E-15	2.189674E-17	1.839127E-05
7.00000	6.267891E-15	1.444985E-17	1.494579E-05
8.00000	5.844278E-15	8.675031E-18	1.158776E-05
8.50000	5.490760E-15	6.931039E-18	1.038272E-05
9.80000	4.319402E-15	4.001894E-18	7.956292E-06
10.30000	3.941371E-15	3.288699E-18	7.231511E-06
11.20000	3.728774E-15	2.363778E-18	6.131645E-06
11.70000	3.544942E-15	2.001574E-18	5.652318E-06
12.00000	3.467633E-15	1.818229E-18	5.391398E-06
12.50000	3.251383E-15	1.566138E-18	5.021032E-06
12.89000	2.932296E-15	1.393372E-18	4.755807E-06
15.00000	2.279837E-15	7.500050E-19	3.496754E-06
17.40000	1.959537E-15	4.177471E-19	2.615318E-06
17.72000	1.923759E-15	3.887121E-19	2.523343E-06
18.00000	1.895113E-15	3.654184E-19	2.447057E-06

19.50000	1.746714E-15	2.668773E-19	2.094133E-06
20.80000	1.631486E-15	2.070066E-19	1.846302E-06
21.00000	1.616373E-15	1.993476E-19	1.812002E-06
21.50000	1.580868E-15	1.817423E-19	1.730740E-06
23.00000	1.481593E-15	1.395495E-19	1.518321E-06
24.50000	1.388212E-15	1.089938E-19	1.343605E-06
25.00000	1.358150E-15	1.007104E-19	1.292112E-06
27.00000	1.249630E-15	7.448243E-20	1.113045E-06
30.00000	1.116508E-15	4.928052E-20	9.073606E-07
31.50000	1.060397E-15	4.069663E-20	8.253473E-07
33.00000	1.010141E-15	3.391371E-20	7.541294E-07
36.00000	9.206467E-16	2.410932E-20	6.370899E-07
42.00000	7.794012E-16	1.315832E-20	4.721886E-07
48.00000	6.868028E-16	7.780689E-21	3.638423E-07
55.00000	6.085655E-16	4.570421E-21	2.796205E-07
60.00000	5.507078E-16	3.252338E-21	2.365525E-07
65.00000	5.044838E-16	2.369792E-21	2.023546E-07
80.00000	4.269617E-16	1.049239E-21	1.347752E-07
100.00000	3.604128E-16	4.394469E-22	8.768929E-08
250.00000	1.401917E-16	1.244246E-23	1.632525E-08
450.00000	7.632064E-17	1.265206E-24	-5.870612E-10
500.00000	6.847541E-17	8.332686E-25	1.105422E-08
900.00000	4.027006E-17	8.026631E-26	5.081451E-09
1100.00000	3.350304E-17	3.603344E-26	1.088198E-08
1400.00000	2.746215E-17	1.377449E-26	4.297113E-08
1600.00000	2.448176E-17	8.086001E-27	7.900457E-08
1900.00000	2.088372E-17	4.070869E-27	2.518963E-07
2200.00000	1.843765E-17	2.268098E-27	-5.919263E-08
2800.00000	1.489648E-17	8.660789E-28	7.366428E-09
3500.00000	1.238304E-17	3.556552E-28	4.555300E-07
4100.00000	1.066987E-17	1.890074E-28	-7.368510E-07
4900.00000	9.041967E-18	9.273289E-29	-6.663277E-07

5500.00000	8.255566E-18	5.851957E-29	-7.216848E-07
6200.00000	7.540664E-18	3.631902E-29	-1.394855E-06
7000.00000	6.753276E-18	2.237210E-29	2.060536E-07
7810.00000	6.180253E-18	1.446353E-29	-1.145263E-06
8700.00000	5.603742E-18	9.402779E-30	2.339741E-06
9200.00000	5.349310E-18	7.525838E-30	2.300566E-06
10000.00000	4.952723E-18	5.394436E-30	9.949888E-07

Appendix B

Spectral Energy Distribution(SED) of data generated by 2- Dust code and ISO Spectra.

Table B.1: Spectral Energy Distribution(SED) taken from the ISO Spectra.

S.N.	Wavelength (μm)	Flux (Jy)	S.N.	Wavelength (μm)	Flux (Jy)	S.N.	Wavelength (μm)	Flux (Jy)	S.N.	Wavelength (μm)	Flux (Jy)	S.N.	Wavelength (μm)	Flux (Jy)
1	4.2	0.01	43	12.6	0.77	85	21.0	3.18	127	29.4	12.34	169	37.8	15.21
2	4.4	0.07	44	12.8	0.05	86	21.2	1.4	128	29.6	13.89	170	38.0	19.29
3	4.6	0.03	45	13.0	0.37	87	21.4	0.84	129	29.8	12.99	171	38.2	23.96
4	4.8	0.6	46	13.2	0.52	88	21.6	0.04	130	30.0	18.16	172	38.4	14.01
5	5.0	0.01	47	‘13.4	1.18	89	21.8	0.08	131	30.2	14.52	173	38.6	9.21
6	5.2	0.03	48	13.6	0.69	90	22.0	0.1	132	30.4	12.96	174	38.8	10.74
7	5.4	0.06	49	13.8	1.12	91	22.2	0.1	133	30.6	12.26	175	39.0	8.71
8	5.6		50	14.0	0.09	92	22.4	0.05	134	30.8	13.46	176	39.2	7.66
9	5.8	0.05	51	14.2		93	22.6	0.05	135	31.0	11.32	177	39.4	10.02
10	6.0	0.01	52	14.4	0.05	94	22.8	0.12	136	31.2	16.1	178	39.6	11.69
11	6.2		53	14.6	0.45	95	23.0	1.15	137	31.4	17.25	179	39.8	14.17
12	6.4	0.07	54	14.8	0.06	96	23.2	0.77	138	31.6	15.09	180	40.0	11.8
13	6.6		55	15.0		97	23.4	0.48	139	31.8	15.79	181	40.2	6.67
14	6.8		56	15.2	0.04	98	23.6	1.49	140	32.0	15.52	182	40.4	12.35
15	7.0	0.08	57	15.4	0.02	99	23.8	1.12	141	32.2	14.28	183	40.6	9.74
16	7.2		58	15.6	0.97	100	24.0	0.45	142	32.4	12.69	184	40.8	14.97
17	7.4		59	15.8		101	24.2	0.4	143	32.6	8.88	185	41.0	6.31
18	7.6		60	16.0	0.07	102	24.4	0.92	144	32.8	11.07	186	41.2	11.72
19	7.8	0.08	61	16.2	0.24	103	24.6	0.67	145	33.0	11.75	187	41.4	11.22
20	8.0	0.01	62	16.4	0.04	104	24.8	1.03	146	33.2	14.28	188	41.6	9.82
21	8.2		63	16.6	0.67	105	25.0	0.96	146	33.4	12.23	189	41.8	9.57
22	8.4		64	16.8	0.02	106	25.2	0.35	148	33.6	14.47	190	42.0	10.31
23	8.6		65	17.0	0.07	107	25.4	0.6	149	33.8	11.25	191	42.2	7.94
24	8.8	0.02	66	17.2	0.26	108	25.6	0.92	150	34.0	16.92	192	42.4	6.12
25	9.0	0.03	67	17.4	0.49	109	25.8	1.44	151	34.2	16.42	193	42.6	7.29
26	9.2		68	17.6	0.06	110	26.0	0.99	152	34.4	19.95	194	42.8	11.98
27	9.4		69	17.8	0.13	111	26.2	1.01	153	34.6	16.7	195	43.0	8.64
28	9.6	0.04	70	18.0	1.16	112	26.4	0.11	154	34.8	13.2	196	43.2	14.04
29	9.8		71	18.2	1.68	113	26.6	0.03	155	35.0	13	197	43.4	22.54
30	10.0	0.02	72	18.4	2.13	114	26.8	0.9	156	35.2	13.18	198	43.6	17.17
31	10.2	0.06	73	18.6	2.25	115	27.0	0.02	157	35.4	12.25	2199	43.8	15.46
32	10.4	0.01	74	18.8	4.38	116	27.2	1.18	158	35.6	12.96	200	44.0	10.03
33	10.6	0.13	75	19.0	1.01	117	27.4	1.29	159	35.8	13.87	201	44.2	21.27
34	10.8	0.03	76	19.2	0.01	118	27.6	4.58	160	36.0	14.46	202	44.4	17.62
35	11.0	0.07	77	19.4	1.73	119	27.8	3.1	161	36.2	14.77	203	44.6	18.63
36	11.2	0.06	78	19.6	0.16	120	28.0	2.49	162	36.4	9.67	204	44.8	20.44
37	11.4	0.17	79	19.8	2.24	121	28.2	5.36	163	36.6	10.71	205	45.0	18.4
28	11.6	0.1	80	20.0	1.29	122	28.4	10.89	164	36.8	9.3	206	45.2	17.61
39	11.8	0.04	81	20.2	0.65	12 3	28.6	5.45	165	37.0	8.97	207	45.4	19.49
40	12.0	0.06	82	20.4	1.12	124	28.8	13.82	166	37.2	12.99			
41	12.2	0.08	83	20.6	0.46	125	29.0	10.51	167	37.4	13.32			
42	12.4	0.02	84	20.8	1.9	126	29.2	7.4	168	37.6	11.36			

Table B.2: Spectral Energy Distribution(SED) taken from the ISO Spectra.

S.N.	Wavelength (μm)	Flux (Jy)	S.N.	Wavelength (μm)	Flux (Jy)	S.N.	Wavelength (μm)	Flux (Jy)
1	1.00 E-1	1.79E-9	25	1.29E+1	1.64E-4	49	2.50E+2	1.33E+2
2	2.00E-1	5.92E-6	26	1.50E+1	2.12E-3	50	4.50E+2	4.78E+1
3	3.65E-1	1.06E-3	27	1.74E+1	2.30E-2	51	5.00E+2	3.91E+1
4	4.50E-1	1.49E-3	28	1.77E+1	3.08E-2	52	9.00E+2	1.25E+1
5	5.56E-1	1.67E-3	29	1.80E+1	3.77E-2	53	1.10E+3	8.10
6	6.40E-1	1.84E-3	30	1.95E+1	1.14E-1	54	1.40E+3	4.75
7	7.90E-1	1.92E-3	31	2.08E+1	2.55E-1	55	1.60E+3	3.477
8	1.25	1.71E-3	32	2.10E+1	2.80E-1	56	1.90E+3	2.27
9	1.65	1.33E-3	33	2.15E+1	3.73E-1	57	2.20E+3	1.58
10	2.20	9.47E-4	34	2.30E+1	7.88E-1	58	2.800E+3	8.50E-1
11	3.45	4.71E-4	35	2.45E+1	1.48	59	3.50E+3	4.78E-1
12	3.75	4.10E-4	36	2.50E+1	1.80	60	4.10E+3	3.10E-1
13	4.80	2.70E-4	37	2.70E+1	3.55	61	4.90E+3	1.90E-1
14	5.20	2.35E-4	38	3.0E+1	8.02	62	5.50E+3	1.40E-1
15	5.80	1.92E-4	39	3.15E+1	1.14E+1	63	6.20E+3	1.02E-1
16	6.30	1.65E-4	40	3.30E+1	1.54E+1	64	7.00E+2	7.29E-2
17	7.0	1.35E-4	41	3.60E+1	2.58E+1	65	7.81E+3	5.42E-1
18	8.0	1.04E-4	42	4.20E+1	5.46E+1	66	8.70E+3	4.00E-2
19	9.0	9.31E-5	43	4.80E+1	9.21E+1	67	9.20E+3	3.43E-2
20	1.03E+1	7.19E-5	44	5.50E+1	1.40E+2	68	1.00E+4	2.71E-2
21	1.12E+1	6.61E-5	45	6.0E+1	1.70E+2			
22	1.17E+1	6.08E-5	46	6.50E+1	1.96E+2			
23	1.20E+1	6.63E-5	47	8.00E+1	2.65E+2			
24	1.25E+1	1.21E-4	48	1.00E+2	3.09E+2			